Quantifying Morphological Changes & Sediment Transport Pathways on Comet 67P/Churyumov-Gerasimenko

M. N. Barrington[1], S. P. D. Birch[2,3], A. Jindal[3], A. G. Hayes[3], P. Corlies[2,3†], and J.-B. Vincent[4]

[1] Department of Earth and Atmospheric Sciences, Cornell University, Ithaca, NY, USA
[2]Department of Earth, Atmospheric, and Planetary Sciences, Massachusetts Institute of Technology, Cambridge, MA, USA. [3]Department of Astronomy, Cornell University, Ithaca, NY, USA.[4] DLR Institute of Planetary Research, Berlin, Germany.

Corresponding author: Megan Barrington (mne8@cornell.edu)

† Current address: Spectral Sciences Inc. 4 Fourth Ave., Burlington, MA, 01803

Key Points:

- Sediment is intra- and inter-regionally redistributed.
- Erosion and deposition follow the subsolar latitude, and are strongly influenced by local topography.
- Scarp activity is primarily limited to equatorial and internal regions.
- We observe net zero erosion/deposition on the tops of the lobes, perhaps indicating the presence of terminal sinks for airfalling sediment.

Abstract

Comets are active geological worlds with primitive surfaces that have been shaped to varying degrees by sublimation-driven sediment transport processes. Rosetta's rendezvous with comet 67P/Churyumov-Gerasimenko (67P) in 2014 provided data with the necessary spatial and temporal resolutions to observe how micro-gravity worlds evolve. Rosetta's observations have thus far revealed that the majority of changes to the surface occurred within 67P's smooth terrains, vast sedimentary deposits that blanket a significant fraction of the nucleus. Understanding the global context of these changes, and therefore the sediment transport pathways that govern the evolution of 67P's surface requires a thorough description of their changing morphologies, and an evaluation of existing global-scale spatial and temporal trends. Accordingly, we present a time-resolved synthesis of erosion and deposition activity on comet 67P as it passed through its August 13, 2015 perihelion from September, 2014 to August, 2016. Our mapping results indicate that, around perihelion, sediment is globally redistributed inter-regionally from 67P's more active south to the north. Equally important, however, are local, topographically-influenced sediment transport processes, with large volumes of sediment moving intra-regionally over sub-kilometer scales. We also show evidence for regions of near-zero net erosion/deposition between approximately 30–60° latitude, which may act as terminal sedimentary sinks, with remobilization of these materials hindered by multiple factors. This work provides a complete mapping of the sediment transport processes and pathways across 67P observed by the Rosetta misison, and represents a critical step toward understanding the global landscape evolution of cometary surfaces.

Plain Language Summary

Comets are some of the oldest materials in the solar system. When these ice-rich bodies approach the sun, the ices at the surface change phase from solid to gaseous. The change in phase of ices at the surface is the primary cause for the breaking of solid materials into smaller bits, as well as the movement of material around and off of the comet's surface. On comet 67P, where boulders, rocks, gravels and finer materials coat most of the northern surface, this phase change can move material in many different ways. Determining how and where materials are moving across the entire comet can help understand how the ice content of the comet may have changed since it formed. Using our observations of the changing geology of 67P, we can make predictions about geologic processes acting on other comet surfaces.

1 Introduction

Comets are composed of primitive materials that once existed frozen in the outer realm of the solar system. These remnants of the earliest era of planetary formation were eventually transported to their current reservoirs through planetary migration and/or interactions with other stars and gas clouds (A'Hearn, 2012). Jupiter Family Comets (JFCs) are of particular interest for scientific study due to their short orbital periods, and close perihelion passages that permit detailed spacecraft observations. Broadly, as these objects migrated increasingly closer to the Sun, their volatile-rich surfaces began to evolve as various ices exposed at the surface sublimated. This process drives the physical and chemical weathering of the consolidated

nucleus, wherein sediment is produced and transported either across, or entirely ejected from, the surface.

Of the five JFCs visited by spacecraft observations to date, four have been sufficiently resolved to permit geological studies of their surfaces. These include 81P/Wild 2 (Brownlee et al., 2004), 9P/Tempel 1 (Thomas et al., 2013a; Veverka et al., 2013), 103P/Hartley 2 (Thomas et al., 2013b), and 67P/Churyumov-Gerasimenko (67P) (El-Maarry et al., 2017). These observations all showed that cometary nuclei are complex worlds, with regions of unconsolidated sedimentary grains coating an otherwise consolidated, rugged nucleus (Sunshine, 2016). Meanwhile observations of comets 19P/Borrelly (Soderblom et al., 2002) and 1P/Halley (Reinhard, 1986), though hinting at similar landscapes, had insufficient resolutions for more quantitative analyses.

Of these five JFCs, the highest spatial and temporal resolution datasets documented comet 67P. Rosetta collected over 8,200 high resolution images of 67P's surface over the span of the mission's two year visit to the comet from 2014 to 2016 (Keller, 2007). These data provide a unique opportunity to observe high spatial and temporal resolution changes occurring on 67P's smooth terrains. Here, the term smooth terrains is used as a catch-all term to describe morphologies which have previously been described as smooth terrains, cauliflower plains, and pitted plains on comet 67P (Birch et al., 2017; Moruzzi et al., 2022). Smooth terrains are composed of sedimentary grains that are likely sourced from the consolidated nucleus, albeit by unknown means. Sublimation of ice within the consolidated nucleus then weathers the nucleus, accelerating liberated particles off the surface. Larger grains then follow ballistic trajectories and fall back to the surface, depositing as 'airfall' in topographical and gravitational lows in the comet's northern latitudes (Fig. 1; Keller, 2017). Airfall grain sizes range from centimeter to decimeter scale (Keller, 2017), and are heterogeneous in both their size distribution (Pajola, 2017) and volatile content (Davidsson et al., 2021) across the surface of 67P. While it was initially hypothesized that these airfall materials would act as an insulating layer that would suppress activity from the more ice-rich layers below (Keller, 1986), Rosetta instead observed that the smooth terrains hosted the majority of large-scale changes. This suggests that the sedimentary grains retain large volumes of volatile ices despite their exposure within the coma during transport. Indeed, Davidsson et al. (2021) found that for a transit time of 12 hours, centimeter sized particles retained ~50% of their original water ice, with decimeter sized particles retaining up to ~90%. More volatile ices (e.g., CO, CO_2), however, are depleted well within typical transit times unless buried within the cores of larger grains.

Past work has documented several types of morphological units on 67P, including consolidated nucleus materials (a.k.a consolidated terrain), which often outcrop in the form of cliffs within smooth terrain regions, as well as bouldered terrains, talus deposits, smooth terrains, cauliflower plains, and pitted plains (Birch et al., 2017). Surface changes that have been examined in detail include depressions (Birch et al., 2017), scarps (Birch et al., 2017, El-Maarry, 2017; Jindal et al., 2022), honeycomb features (Shi et al., 2016; Hu et al., 2017; El-Maarry et al., 2019), ripples (El-Maarry et al., 2017; Jia et al., 2017), pits (Deshapriya et al., 2016), and bright spots (Deshapriya et al., 2016; Fornasier et al., 2016). Although these many studies documented the evolution of isolated regions and features on 67P, a synthesis of the evolution of all of 67P's smooth terrains has remained unexplored. Thus, it is necessary to study the global geologic processes which have acted on 67P, a task that will have broad implications for cometary surfaces more generally as smooth terrains appear ubiquitous across all of the cometary nuclei imaged with sufficient resolution to identify them. Herein, we present a synthesis of the

sublimation-driven surface evolution and sediment re-distribution of the smooth terrains of comet 67P.

2 Methods

We utilized images collected by Rosetta's Optical, Spectroscopic, and Infrared Remote Sensing Imaging System (OSIRIS) Near Angle Camera (NAC), which acquired over 8,200 images of the surface of comet 67P. These data document both the coma and the surface of the comet before, during, and after 67P's 2015 perihelion passage. Previous mapping of 67P (El-Maarry et al., 2015; Thomas et al., 2015) documented smooth terrain deposits across the comet, with most deposits found in 67P's northern hemisphere (Birch et al., 2017; El-Maarry et al., 2015). For portions of the comet containing known smooth terrains, we divided them into 25 distinct sub-regions, with naming conventions based on the nomenclature from El-Maarry et al. (2015) (Fig. 1). This subdivision was done out of necessity because of (1) the comet's complex geometry, (2) data quality variations, (3) data coverage gaps, and (4) the vast latitudinal and longitudinal expanse of several previously defined (El-Maarry et al., 2015) regions. Despite various attempts to generate an automated image processing pipeline, we determined that manual image selection was the most efficient way to find images that: (1) met resolution requirements, (2) displayed a significant portion of a given region under investigation, (3) did not display locally saturated data, and (4) provided optimal viewing geometry and phase angles for detection of 1–10 meter scale changes. To reduce errors in change detection due to variations in viewing geometry, phase angles between 45–90° were preferentially selected for image analysis, with >90% of images falling within this range (Table S1). Due to inconsistent coverage of each region, more extreme phase angles were also utilized as necessary when higher quality observations were not available (Table S1).

Our method of manual image selection, projection, and change detection was performed in multiple steps. First, reference images were manually selected for each sub-region as early as data coverage of each region allowed. Next, follow-up images of each sub-region were selected, initially at a cadence of once per month after the date of their respective reference images. If changes were detected between two consecutive images at this cadence, the image cadence was increased systematically until either no further changes were detected between consecutive images, or until coverage of the region was not available at a shorter interval of time. Whenever possible, we leverage multiple images of a given surface change, though sporadic coverage and changing resolution/imaging conditions meant such confirmations, as well as precise determinations about the dates on which changes began/ceased were not always possible (yellow boxes in Table S3).

For each sub-region, we then projected each image into the frame of our reference image using the ShapeViewer (www.comet-toolbox.com) software package (Vincent 2018). This allowed us to blink images and more reliably detect finer-scale changes and their precise locations than what would otherwise be possible by analyzing unprojected images side-by-side. ShapeViewer also allowed for viewing high-resolution, small field-of-view images in a global context, aiding in our later interpretations. Finally, for each region, mapping of all changes was performed in the ArcGIS software as shapefiles and layers. Identified changes, each confirmed by at least two individual mappers, were annotated and analyzed for 619 images in total (Table S1) with resolutions ranging from approximately 0.1–20 m/pixel. If necessary, the contrast and brightness of each image was adjusted to provide better perspective for the interpretation of

possible changes in each image. Measurements of distance and feature size were made in ArcMap by converting an arbitrary unit to meters using scale bars created during layer generation in Shapeviewer.

It is important to note that data coverage was incomplete, especially near perihelion from mid- to late-2015 as the Rosetta spacecraft backed away from the comet. This resulted in images having far coarser resolution during these most active periods. Images also had variable phase angles and illumination conditions, further complicating our search for changes. For example, data over 67P's northern latitudes were progressively more difficult to use, eventually becoming unusable when those latitudes entered polar winter (black boxes in Table S3). Resolution limitations were addressed first by including estimated uncertainties (yellow boxes, Table S3) between dates when changes were observed and the earliest date a change may have occurred before our observation. Next, wherever possible, observations were confirmed in sequential images. Whenever a candidate change was unclear due to poor resolution, the changes were flagged as 'low-confidence' observations (Table S2), and were not included in the synthesis of activity in the northern hemisphere. Sequential images whose average phase angles vary by greater than 45° were also flagged in Table S1. Therefore, while we know our mapping is incomplete near perihelion and for scales below ~1 meter, our consistent image selection, projection, and stretching routine allowed us to place constraints on when we were certain activity occurred in a given region (green boxes in Table S3) and when it was possible, but not confirmed that activity occurred (yellow boxes in Table S3). We accordingly specify that observations occur by a specific date to indicate the latest possible date on which a change occurred, as limited by either resolution, shadows, viewing geometry, or data coverage.

We identified and searched for six types of changes in each of our 25 sub-regions. These changes included boulder burial, boulder exposure, boulder migration, scarp migration (Fig. 2), plains migration (Fig. 3), and honeycomb evolution (Fig. 4). See Table S2 for a complete catalog of detected changes. For the purposes of our work, boulder burial includes only boulders that were totally covered by the deposition of new smooth terrains (Fig. 2), as varying illumination conditions and distortions inherent to the projection of images complicated our ability to interpret any partial burials. Boulder exposure likewise describe boulders which had been completely covered by smooth terrains and were later revealed, but does not include already exposed boulders undergoing further local erosion for the same reasons as above (Fig. 2). Exposures and burials of outcrops of the underlying consolidated nucleus were interpreted similarly to their boulder counterparts and were classified in these same categories for simplicity. Boulder migration documents the movement of boulders ranging from meters to tens of meters in diameter within talus deposits and boulder fields, falling from local cliffs, or those being emplaced from regions beyond individual image boundaries (i.e., the initial boulder location is not known). Differentiation between boulder exposures and boulder migrations were typically made based on two factors: 1) Previous indication(s) of a boulder's presence. Visible evidence of boulders beneath the surface sediment, such as mounds of sediment where a boulder is later exposed, are all classified as boulder exposures. 2) The boulder's proximity to talus deposits. If the pre-existing location of a boulder cannot be determined, the boulder is classified as migration when located within or proximal to a talus deposit. If distal from any talus deposit or cliff within the center of a smooth terrain deposit, we instead classify as boulder exposures. One exception is the ~10 meter scale boulder that migrated from an unknown cliff into Hapi 1 (Fig. 2), distinguished by slight impact impressions near the new boulder in the center of the region.

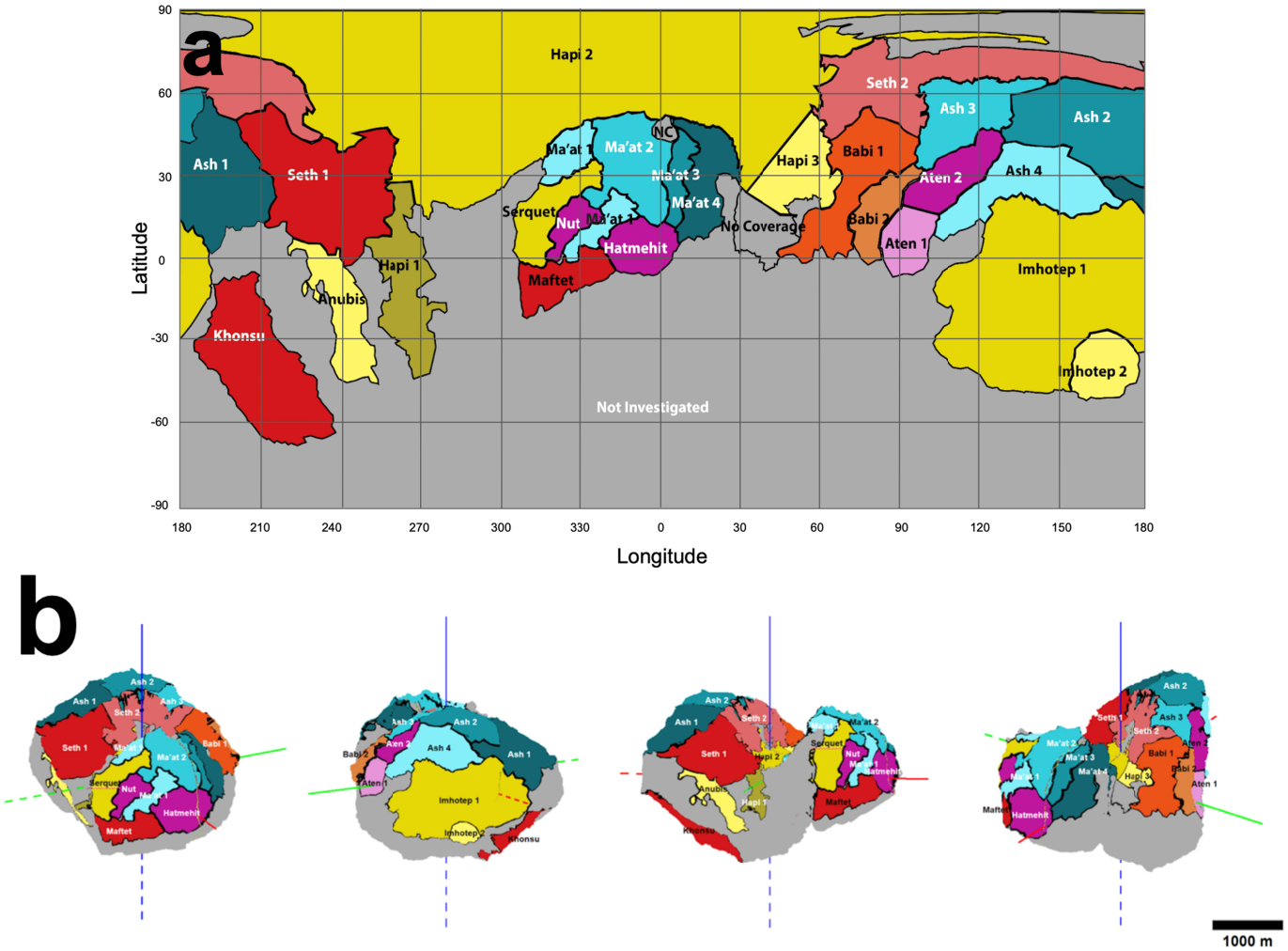

Figure 1. **a)** An equirectangular projection of our 25 sub-regions of smooth terrains analyzed for surface evolution. Colored regions are dominated by smooth terrains, while the regions in gray show few smooth terrains, instead being dominated by consolidated materials. Gray regions were not considered in our work. Regions labeled 'No Coverage' and 'NC' were not investigated due to insufficient coverage in reference images. **b)** Four orientations of a 3D projection of 25 sub-regions of smooth terrains on 67P. X-Axis: Red, Y-Axis: Green, Z-Axis: Blue. Dashed lines represent negative axis directions.

Scarp migration describes the formation and/or subsequent movement of arcuate or semi-arcuate depressions (Fig. 2), all of which are bounded at least on one side by a migrating scarp wall. These depressions are typically observed migrating radially from a topographic discontinuity, although the genesis point is not always clear (Birch et al., 2019; Jindal et al., 2022). The radial migration of the scarps is key in differentiating between the processes of scarp migration and plains migration.

Plains migration describes the re-distribution of sediment deposits which form mounds or dune-like crests (Fig. 3; Thomas et al., 2019). We detected this process by analyzing the movement of these mounds and crests, identifying variations in surface roughness, and/or observing changing locations of the boundaries between smooth terrains and neighboring consolidated regions.

Finally, honeycomb evolution describes the increase or decrease in surface roughness of "honeycombs" (Hu et al. 2017; Shi et al., 2016; El-Maarry et al., 2019). These ten meter scale, highly textured areas form just beneath some smooth terrains. As such, they experience a reduction in surface roughness when new granular materials are deposited, and an increase in roughness when overlying material is eroded (Fig. 4; Shi et al., 2016).

In addition to the six broad types of change described above, several additional isolated types of changes were observed throughout the mission. These include the formation of bright, likely ice-rich, pits in Khonsu (Fig. 5; Deshapriya et al., 2016; Fornasier et al., 2015; Oklay et al., 2016), the destruction and subsequent reformation of a set of ripple bedforms in Hapi 1 (Fig. S2; El-Maarry et al., 2017; Jia et al., 2017), and quasi-circular pits that appear in Ash 1.

We classified each type of change into categories of erosion, deposition, or re-distribution for the synthesis of global sediment transport trends and sorted into sequential three-month time bins beginning in August, 2014 and ending in August, 2016 (Table S3; Fig. 6–8). The first three time bins are Pre-Perihelion 1, 2 and 3. Images from these time bins were taken before 67P's August 2015 perihelion. The next two time bins, Near-Perihelion 1 and 2, group images collected a few months before, during, and a few months after perihelion. Finally, images grouped into the last three time bins, Post-Perihelion 1, 2, and 3, were taken after 67P had passed perihelion.

Each Scarp migration, boulder/nucleus exposure, boulder migration, increased surface roughness in honeycombs, and pit formation in Ash and Khonsu are all classified as erosional processes. All these processes act to remove granular smooth terrain material on the surface, most likely driven by the sublimation of near-surface volatile ices (Hu et al., 2017; El-Maarry et al., 2017; Birch et al., 2019; Jindal et al., 2022). We classify boulder burials, nucleus burials, and decreased surface roughness of honeycombs as indicators of deposition of new smooth terrain sediment. While other research classifies the burial of scarps as a depositional indicator (Jindal et al., 2022), we did not include them here due to the difficulty of classifying fading scarps with varying viewing geometries. However, we still used scarp fading/burial to better interpret trends in our data when appropriate. Finally, the reformation of ripples in Hapi 1, as well as the general migration of plains are classified as redistributions of sediment. We specifically classify these separately because, though we know changes occurred, we cannot conclude whether erosion or deposition occurred (or both) due to the lack of nearby topographic benchmarks like boulders or the underlying nucleus. For example, the migration of plains materials and dune-like crests clearly show movement of granular materials, but the movement could be due either to small impacts splashing particles on the surface downslope (Thomas et al., 2015), or due to ice sublimation in the near surface moving small volumes of materials.

3 Results

3.1 Pre-Perihelion Activity

3.1.1 Pre-Perihelion 1

The earliest onset of activity occurred as limited erosion within Hapi 1 during Pre-Perihelion 1 (September–November, 2014). Two boulders were exposed in the center of the region on September 12, 2014. We also observed the potential migration of features analogous to aeolian ripples (El-Maarry et al., 2017; El-Maarry et al., 2019; Davidsson et al., 2015; Jia et al., 2016) in Hapi 1 from September 2–September 12, 2014, although this initial change in position may be an artifact of the image projection process. Barucci et al. (2016) first described the presence of bright patches during this epoch, which they interpreted to be spectrally bright due to the presence of water ice. These patches occurred as individual boulders/patches in a western alcove of Imhotep 1 and in Imhotep 1's eastern pitted region (Barucci et al., 2016), and as a cluster at the boundary of Imhotep 1 and Apis (Barucci et al., 2016; Oklay et al., 2016). These specific features persisted for months, although lifespans of other bright spots varied (Barucci et al., 2016). We did not search for instances of bright patches in this work, as they often occurred at boarders between consolidated and smooth terrain regions. We detected no erosional or depositional activity associated with these spectral changes.

3.1.2 Pre-Perihelion 2

Erosion, deposition and re-distribution of smooth terrains began in earnest during Pre-Perihelion 2, from December 2014 until February 2015 (Figure 4). We detected scarps migrating within Hapi 2, Hapi 3 and Seth 2 by December, 2014 and within Seth 1 by January 23, 2014. The migrating scarps within Hapi 2 are of particular interest during this epoch, as large quasi-arcuate scarp fronts emanated from 67P's north pole toward Hapi 1 and Hapi 3 between December 30, 2014 and February 9, 2015. While scarp migrations were recorded in the Hapi region by El-Maarry et al. (2017), we show here that they began at least one month prior to their observations. These scarp migrations continued through February, 2015 within Seth 1, Seth 2, Hapi 2, and Hapi 3. We also observed boulder exposures in Ash 3, Hapi 3, and possibly in Hapi 2. In Ash 3, two boulders were exposed by December 2, 2014. Much greater erosion appears to have occurred within Hapi 2, as migrating scarps exposed five boulders on December 30, 2014, and another 16 by January 22, 2015. With the exception of Ash 3, we consider all of these regions to be "internal", meaning they are all located directly within the neck, or they are near the neck region and have a significant portion of their surface tilted toward the Hathor cliff. While many of these regions are proximal to the neck, our observations clearly show that erosional activity also expanded south of (away from) the neck.

Hu et al. (2017) and El-Maarry et al. (2019) described honeycombs that began to evolve in Ma'at by January 22, 2015, and in the Nut and Serqet regions by February 14, 2015, including depressions that would later mature into honeycombs. Our own observations indicate the large-scale redistribution of smooth terrain materials within Ma'at 4 on February 21, 2015.

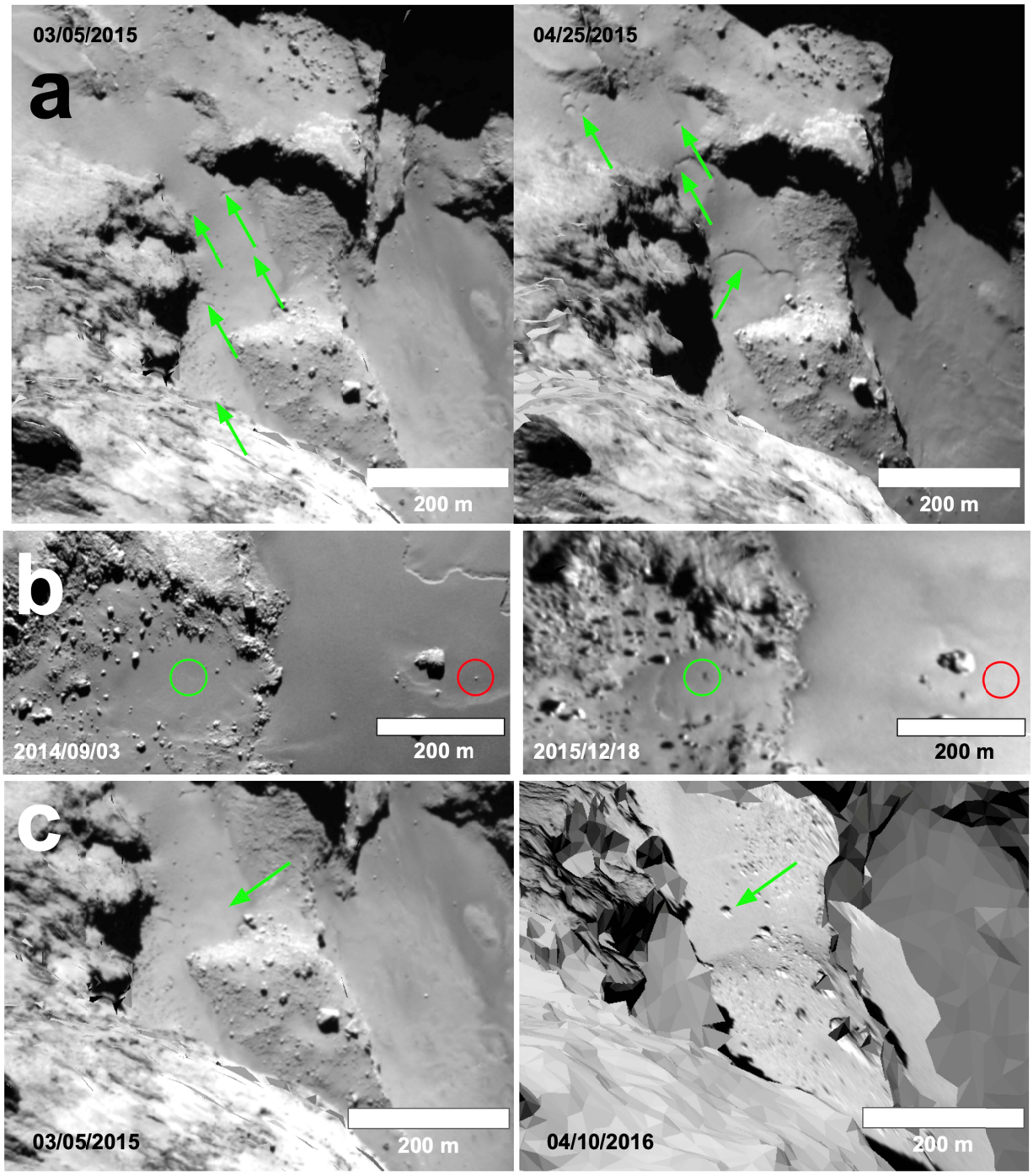

Figure 2. a) Co-registered images of Hapi 1 showing arcuate scarp fronts migrating (green arrows) between March 5 and April 25, 2015. **b)** One boulder exposure circled in green and one boulder burial circled in red, seen in Imhotep 1. **c)** One boulder sourced from an unknown location migrating into Hapi 1, with notable depressions nearby suggesting it bounced twice.

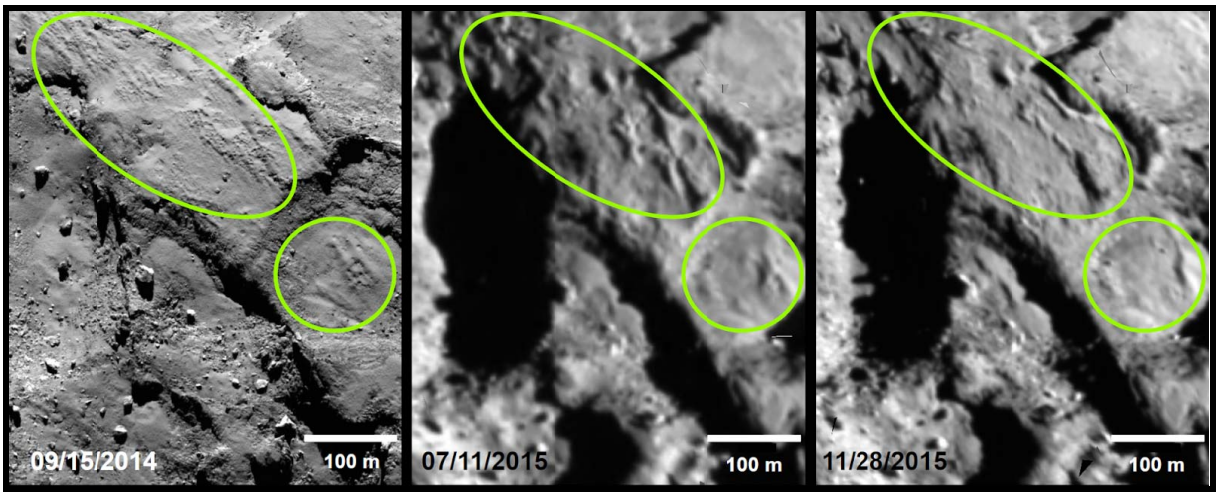

Figure 3. Co-registered images showing migrating sediment plains in Maftet.

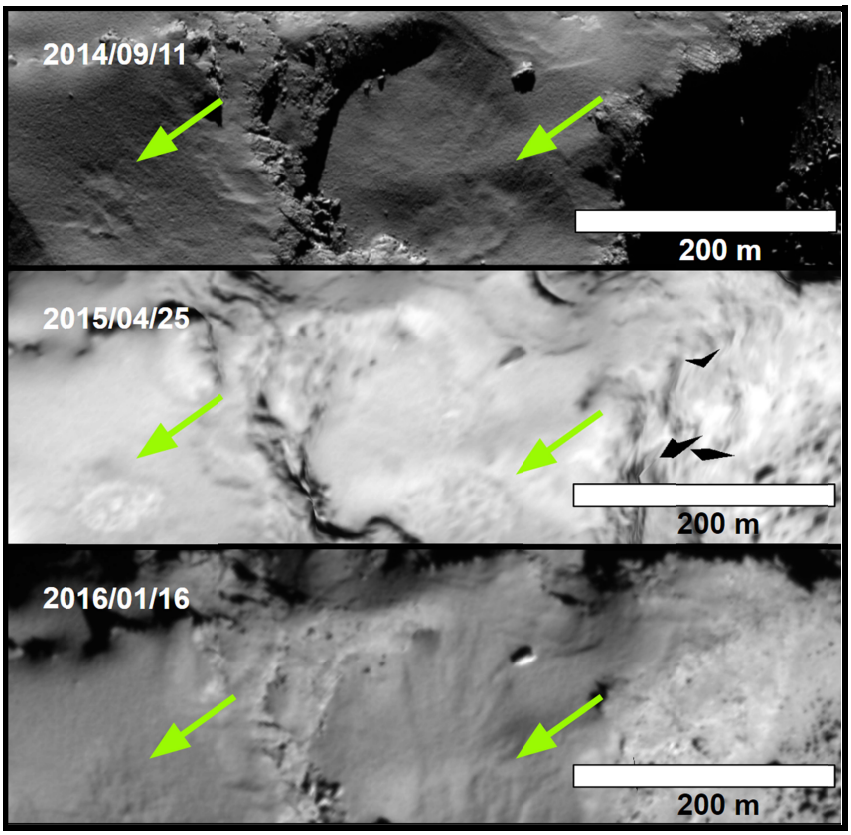

Figure 4. Co-registered images showing evolving honeycomb structures in Seth 1.

We searched for and located many evolving honeycomb features throughout the mission, however our image processing sometimes limited our ability to clearly discern such detailed changes in surface expression. In the case of the depressions on the Ash/Seth border, as well as honeycombs in Serqet, this led to a later detection date in our dataset (~1 month). However, we did often detect the large-scale migrations of plains and crests within smooth terrains, as described above within Ma'at 4, and which we also identified in Seth 1 (January 23, 2015), Seth 2 (December 12, 2014) and Hapi 1 (February 14, 2015).

We also discovered the first clear evidence of deposition of new smooth terrain materials in Hatmehit, Ma'at 4, Babi 2, Aten 1 and Aten 2 (Figure 4) In February of 2015, regions which are located generally south of the initial erosion activity dominated by Hapi 2 and Hapi 3. We identified isolated instances of boulder and nucleus burials within Babi 2 and Hatmehit on February 19 and February 20, 2015, respectively. The most significant and obvious deposition occurred in Ma'at 4 on the comet's small lobe. In this region, the newly deposited material covered at least 11 large boulders and numerous nucleus outcrops that span the width of the entire sub-region by February 21, 2015. This early deposition marked the beginning of a widespread deposition event which continued in Ma'at 4 and in neighboring regions of Ma'at for several months. Notably, this depositional event over a significant portion of the small lobe coincided precisely with erosional activity in the Hapi 2 region. Hapi 2 is proximal to Ma'at 3 and 4, lying just to the north in the deep gravitational low of the neck, perhaps indicating a causal relationship.

3.1.3 Pre-Perihelion 3

During the next epoch, Pre-Perihelion 3 (March–May, 2015), erosional activity continued to expand southward, including within the low and mid-latitudinal regions of Ash 1, Ma'at 4, and Babi 1. We observed numerous migrating scarps within a highly localized, low latitude area of Ash 1 on April 22 and May 16, 2015. Each scarp appeared to expand radially in an eastward direction, and emanated from the base of a local cliff. We detected polygonal scarps migrating within Babi 1, an internal sub-region of Babi (Fig. 1), from March 14–May 10, 2015. We first saw scarps appear on terraces proximal to the neck in March, followed by the expansion of these scarps and the formation of a new polygonal scarp in a northern terrace of the region by April 19, 2015. We also identified a scarp expanding in the southernmost active terrace of Babi 1 by May 10, 2015. Hu et al. (2017) also recorded two small scarps migrating in Ma'at 3 by March 28, 2015 which exposed part of the underlying nucleus.

We observed the continued migration of 10–100 meter scale scarps within Hapi 1, 2, and 3 throughout March–May (Birch et al., 2019; El-Maarry et al., 2017; El-Maarry et al., 2019), as many more irregular scarp fronts formed within the three regions. Although Birch et al. (2019) recorded the last day of scarp migration in Hapi 1 to be April 22, 2015, we detected activity up to one month later on May 23, 2015. During the sequence of scarp activity within the neck, we observed the destruction of the ripples by radially expanding scarps within Hapi 1. These scarps first traveled through the region on April 25, 2015, consistent with the observations of El-Maarry et al. (2017; 2019). Scarp migration began in Seth 1 and Seth 2 by March 5, 2015, and continued into April, 2015, coinciding with the redistribution of sediment in these regions. We found further evidence of erosion by the exposures of four boulders within Hapi 1, and three boulders within Seth 1 on April 25, 2015. Additionally, we observed the exposure of the underlying nucleus in Ma'at 4 and sediment slumping in Ash 1, both by May 16, 2015.

Honeycombs matured within Serqet, Ma'at 3, and Seth 1 (indicated by an obvious increase in surface roughness) on March 5, March 28, and April 25, 2015, respectively. Hu et al. (2017) also recorded honeycombs evolving in Babi 2 by late March, 2015. Both El-Maarry et al. (2017; 2019) and Hu et al. (2017) identified maturing honeycombs in Serqet, consistent with our own observations in Ma'at 3, as well as those of Shi et al. (2016). Barrucci et al. (2016) and Deshapriya et al. (2016) also described the evolution of one bright patch in Khonsu, which persisted from March 10 to May 22, 2015. These observations indicate that the magnitude and

spatial coverage of erosional activity expanded greatly southward as 67P approached equinox in March, 2015.

Deposition also greatly expanded during this period. We identified various combinations of nucleus and boulder burials in Serqet and Maftet by March 5, 2015, in Hapi 1 Hapi 2, Ash 1, Ash 3 and Ma'at 4 by April, 2015, and within Seth 1, Serqet, Ma'at 2, Ma'at 3, Ma'at 4, and Imhotep 1 by May, 2015. We detected at least 56 instances of boulder or nucleus burials from March–May, 2015, as well as the burial of a small circular depression in Serqet (May 10, 2015). Erosion and deposition appeared to be occurring simultaneously in several regions during this epoch. This pattern suggests that either (1) local sediment fallback from smooth terrain erosion was working in tandem with the generation of new sediment in the southern hemisphere to reshape the north, and/or (2) transport distances of sediment within smooth terrains occurred over short, sub-kilometer distances.

3.2 Near-Perihelion Activity

3.2.1 Near-Perihelion 1

As the comet approached perihelion, significant gaps in data arose due to Rosetta's orbital configuration. During Near-Perihelion 1 (June–August, 2015), primarily only low latitudinal external (i.e., non-neck or Hathor-facing) regions were analyzed. Hapi 1 and Seth 1 were the only internal regions with favorable viewing conditions at this time. In Hapi 1, the earlier group of migrating scarps continued, with two larger scarps approaching and merging with one another between June 27, and July 19, 2015. A ~250 m wide scarp progressed away from the rotation axis, and a scarp shaped like a shepherd's crook unfurled and expanded through the initial location of the aeolian ripples. The two scarp fronts merged on July 19, 2015. Interestingly, we detected the aeolian ripples re-forming at least two distinct crests inside the curved shepherd's crook-shaped scarp, on July 11, 2015 (Fig. S2), several months prior to observations by El-Maarry et al. (2017; 2019). One week after the initial ripple re-formation, a third visible crest formed inside the shepherd's crook-shaped scarp, although the crest positions did not reach their final location until the next epoch. This suggests that these crests (or the intervening relative "anti-crests") have a preference for this location on 67P, perhaps analogous to the pit chains on Phobos (Hortsman & Melosh, 1989). One isolated scarp formed in Seth 1, on June 17, 2015, but no further activity was visible in the region.

We detected varying degrees of erosion in the external regions Ash 4, Hatmehit, Anubis, and Imhotep 1. The most notable activity in Near-Perihelion 1 occurred in Imhotep 1, which includes the primary basin on the large lobe, as well as the western and southwestern alcoves. Within the primary basin and the western alcove, we observed numerous scarp fronts migrating tens to hundreds of meters over the duration of the epoch, specifically on June 5, June 27, July 11, July 26, August 1, August 9, and August 23, 2015, consistent with the observations of Groussin et al. (2015) through July 2015. Jindal et al. (2022), recorded the onset of scarp migrations in Imhotep 1 two days prior to our observations, on June 3, and measured an average rate of migration between June 3 and June 27 to be ~23 cm/hr, with migration rates varying between scarps. As the comet drew closer to perihelion (August 13, 2015), scarp activity trended southward, following the subsolar latitude (Jindal et al., 2022). This included the formation of a curvilinear scarp in the southwestern alcove of Imhotep 1 on July 26, 2015 which expanded further south on August 1, 2015. This activity marked the onset of scarp formations and migrations that expanded across the entire Imhotep 1 basin for a brief, but extremely dynamic six

month window of time. Barrucci et al. (2016) also recorded the presence of a short-lived bright patch on the eastern periphery of Imhotep 1, coinciding precisely with the onset of the region's scarp activity. The patch persisted from June 5–27, 2015, waning from a diameter of 36–57 meters. Barrucci et al. (2016) also noted that bright patch production peaked during this epoch, approximately at perihelion, lending credence to their erosional origins.

We identified a scarp front expanding within the pre-existing scarp in Anubis' northern region from July 11–August 1, 2015, and a boulder migrating within an area of coarser sediment farther north on July 26, 2015. We detected two scarps which formed In Ash 4, located north of Imhotep 1 on the face of the large lobe, on June 13, and July 18, 2015, emanating from a western cliff at the edge of the basin. The scarps then migrated eastward and merged on August 9, 2015. While we did not observe scarp migrations in Hatmehit, we did see one boulder migrate ~10 m on July 7, 2015, and a patch of plains in the west migrating from June 27–July 7, 2015. Interpreted together, these processes are consistent with local erosion. Plains migrated in several regions across the northern hemisphere, including Serqet (June 25, July 4, 2015), Ash 1(July 1, 2015), Maftet (July 11, 2015), Hapi 1(July 11, July 25, 2015), and Ash 4 (July 18, August 9, 2015). We also found plains migrating in Maftet, which substantially remodeled the distribution of its smooth materials well into Pre-Perihelion 2, though we lack the high-resolution data necessary to precisely determine the end date of this surface activity. On July 11, 2015, one honeycomb feature located amongst Maftet's migrating plains began to change shape slightly as the smooth terrains were locally re-distributed, although it is unclear if the feature's surface roughness visibly changed on this date.

Another notable erosional event during this period occurred in Seth 2. A cliff previously referred to as 'Aswan' (Pajola et al., 2016) collapsed at the edge of Seth 2's large, flat terrace (Pajola et al., 2017; El-Maarry et al., 2019). The collapse was first identified on July 15, 2015 and created talus deposits which landed on a sediment-covered plateau at a lower elevation, within Hapi 2. Pajola et al. (2017) measured boulders ≥1.5 m before and after the cliff collapse to have increased from ~12,000 to ~18,000.

The only observable deposition that occurred in this time period was detected in Imhotep 1. A meter-scale boulder was buried within the primary Imhotep basin on July 26, 2015. While we did not use the burial of scarps to detect deposition, Jindal et al. (2022) detected the burial of one scarp on July 11, 2015, three scarps on July 26, 2015, a pit on July 31, 2015 and one final scarp on August 6, 2015, indicating that deposition was still occurring during the peak of 67P's erosional activity. This conclusion is particularly supported by images from the weeks after perihelion (23 August–4 September, 2015), as actively migrating scarps were buried by fresh deposition (Jindal et al., 2022). This likely indicates a point at which net local deposition outpaced local erosion in the Imhotep 1 basin. Some of these freshly-deposited smooth terrains may also represent grains that could not escape 67P after being ejected by nearby scarp migration activity.

3.2.2 Near-Perihelion 2

Resolution decreases further during Near-Perihelion 2 (September–November 2015), with only about half of the regions sufficiently imaged for analyses. Even with such limited information, we see extensive changes to 67P's smooth terrains. Scarps continued to migrate within Imhotep 1, first appearing only in the southern portion of the region on September 2, 2015, then expanding again into the northern hemisphere on October 26 and November 21, 2018. A ~100 meter scale scarp migrated south between September 2 and November 21, 2015,

exposing a meter scale boulder in the process. We observed no further scarp migration in Imhotep 1 after November 28, 2015, although Jindal et al. (2022) documented the migration of one final scarp in December, 2015. We did identify a migration of the northern, pre-existing scarp front in Anubis on September 15, 2015. By November 28, 2015 both the northern and southern hemispheric scarp fronts remaining in Anubis from 67P's previous perihelion approach migrated. These two scarp migrations were described by El-Maarry et al. (2017; 2019), although they detected these changes in June, 2016. Several smaller scarp fronts within and around these two larger features also migrated by November 28, 2015, indicating widespread erosion across the region. These observations are all coincident with the location of the subsolar latitude.

We identified additional evidence of erosion in Aten 1, where four boulders migrated by November 28, 2015, and in Maftet, with sediment continuing to redistribute, exposing one boulder and causing two others to migrate. This local redistribution began in July, 2015, with new crest positions observable as late as February, 2016. During this redistribution process, a ~50 meter long pit formed in the southern area of Maftet on November 23, 2015. We also discovered plains migrating within Anubis (September 15, 2015), Hatmehit (November 7, 2015), Ma'at 4 (November 12, 2015), and Imhotep 2 (November 21, 2015). The most drastic of these changes occurred in Imhotep 2 and Maftet, although our resolution limits us from observing whether the plains within Maftet evolved as rapidly or over longer periods as Imhotep 2. Interestingly, in Anubis the freshly liberated sediment from the erosion described above appears to have redistributed within the same region, burying at least one boulder by November 28, 2015. Similarly, material lofted from within Imhotep 1 appears to have landed southeast in Imhotep 2, burying a small boulder in the western plains on November 21, 2015.

We found no further evidence of deposition during this epoch, however Jindal et al. (2022) did observe local deposition in Imhotep 1 by tracking disappearing scarp fronts, noting an interesting change in activity during the weeks following perihelion. They tracked the partial and complete burial of 6 scarps, even as some scarps continued to migrate. This suggests that while deposition and erosion were happening in Imhotep 1 simultaneously, the rate of local deposition across the primary basin began to overcome the rate of local erosion by about November 29, 2015 (Jindal et al., 2022).

3.3 Post-Perihelion Activiy

3.3.1 Post-Perihelion 1

By Post-Perihelion 1 (December, 2015–February, 2016), Rosetta returned to its lower altitude orbits, which improved resolution sufficiently to view much of the comet surface in detail once again and observe any changes that took place throughout perihelion. The most evident erosion first detected during this period occurred on the small lobe, particularly in Ma'at 1, Ma'at 2, and Ma'at 3 from December, 2015 to February, 2016. In addition, we observed several boulder migrations and the formation of quasi-circular, ~5 meter diameter pits in Ma'at 2 on January 17, and February 27, 2016. We do not interpret these pits to be scarps because they did not migrate or expand after their initial formation. Similar features formed within Ash 1 during Post-Perihelion 2 (described below). Significant erosion also occurred in regions neighboring Ma'at by Post-Perihelion 2. We detected three boulder exposures and three boulder migrations west of Ma'at 1, in Nut by December 20, 2015. As resolution increased further, we observed two more boulder migrations, and 22 boulder exposures, generally in the northern half of the region, on February 27, 2016. Further to the west, in Maftet, the only direct evidence of

local erosion came from one boulder migration, which we detected on January 23, 2016. On the face of the small lobe, we identified only limited scarp activity within Hatmehit, where one linear scarp and one curvilinear scarp both expanded southward on December 17, 2015. Five boulders were also exposed across the western half of the region by February 27, 2016.

We only observed evidence of erosion in isolated regions on the large lobe during Post-Perihelion 1. The dynamic activity of Imhotep 1 occurring closer to perihelion did not persist. We observed the exposure of circular pits from beneath a sedimentary cover in the eastern region of Imhotep 1 by February 2016, consistent with El-Maarry et al. (2017; 2019). The most significant erosional changes on the large lobe occurred within Khonsu, located southeast of Imhotep 1 (Fig. 1). Activity within Khonsu began by December 18, 2015, where a boulder ~40 m in diameter migrated ~170 m northward, carving a scar into the nucleus (El-Maarry et al., 2017). Vincent et al. (2016) describe two possible outbursts which may have triggered the downslope rolling of this massive boulder on August 1, 2015 (Near-Perihelion 1), and on September 14, 2015 (Near-Perihelion 2), indicating that the boulder could have migrated earlier than either El-Maarry et al. (2017) or our own observations suggest. Four scarps also migrated in a patch of smooth terrains located in the northern portion of Khonsu, exposing three boulders along their paths on December 18, 2015. One boulder in the same area and a second boulder located in the center of Khonsu also migrated on this date. Four more boulders migrated across the region, and another five boulders were exposed by migrating plains by January 23, 2016.

Three bright pits formed in a central region of Khonsu's smooth terrains on the same date (Fig. 5). The pits appear to have been pre-existing, sediment-mantled structures that were further excavated. Previous analyses suggested that the fresh layer revealed in this process was rich in both water ice and other refractory materials (Deshapriya et al., 2016), (Fornasier et al., 2015), showing spectral similarities to other erosionally active smooth terrains (Deshapriya et al., 2016; Oklay et al., 2016). The pits waned in overall brightness and area over the rest of the mission, however some excess brightness is still detected on July 30, 2016 (Post-Perihelion 3), the last day the they were imaged by the Rosetta spacecraft. It is possible that these pits are analogous to bright spots described by Barucci et al. (2016) and Deshapriya et al. (2016). Deshapriya et al. (2016) described two such bright spots in the Khonsu region. The first (bright spot 2) is located on a "boomerang" shaped feature, and persisted from January 23, to June 24, 2016, while the second (bright spot 3) likely had a much shorter lifetime, as it was only observed once on February 10, 2016. Deshapriya et al. (2016) also correlated the presence of bright spot 2 with an outburst which occurred on August 1, 2015 (Vincent et al., 2016), which may indicate that it persisted for almost one year. Similar to the bright pits, Deshapriya et al. (2016) found that the spectra of the bright spots indicated that they were enriched in water ice.

To the northwest, eight boulders were exposed by migrating smooth terrains in Imhotep 2 on January 23, 2016, after which date we saw no further activity in the region. We detected boulder migrations in Aten 1 on December 2, 2015, and in both Aten 1 and 2 on January 17, 2016, after which no further changes in either region occurred. We identified widespread erosional activity southeast of Aten 2, in Ash 4, as six boulders across the region were exposed and one migrated by December 26, 2015. However only one isolated boulder was exposed in Ash 3, north of Aten 2, by December 2, 2015. Similarly, we located one boulder exposure in Babi 2, the external section of Babi west of Aten 1, on December 26, 2015, and the evolution of a pit field in a southeastern alcove of the region by February 27, 2016. We also identified limited erosion within Babi's internal section, Babi 1, although this is one of the few regions in which scarp migrations were still taking place. In Seth 1, another internal region, we detected two

boulder migrations. We found slightly more activity in Seth 2, as the boundaries of scarps bordering the primary terrace migrated and new talus was deposited in two terraces on January 17, 2016. In the neck, Hapi 2 was in polar winter, and was infrequently imaged over this period of time, preventing our search for surface changes. We did, however, observe active erosion in Hapi 1 and Hapi 3. Seven boulders were exposed, and one boulder migrated within a consolidated area on the eastern periphery of Hapi 1, on December 2, 2015. We detected two more boulder exposures in Hapi 1 on January 9, 2016 with improved image resolution. One week later, we identified one scarp migration, and two small boulder exposures in Hapi 3.

The migration of plains largely coincided with ongoing erosional processes. We observed migrating smooth terrains in Ash 4 (December 2, December 26, 2015), Ma'at 1 (December 2, 2015), Khonsu (December 18, December 31, 2015, January 23, 2016), Nut (December 20, 2015, February 27, 2016), Ma'at 2, (January 17, February 27, 2016), Ma'at 3 (January 17, February 27, 2016), Imhotep 2 (January 23, 2016), Maftet (February 10, 2016), Hatmehit (February 27, 2016), and possibly Babi 2 (December 2, 2015).

We also observed deposition across several regions at this time. We detected two boulder burials in a western strip of Ash 4's smooth terrains on December 2, 2015. We also identified two boulder burials in Ma'at 1 on the same date, three more within Ma'at 3 by January 17, 2016, and four boulder burials in Nut by February 27, 2016. Newly deposited material buried an exposed cliff on the western rim of Imhotep 2 on January 23, 2016, the same area in which a neighboring boulder was buried during the previous epoch. One boulder was buried within Khonsu on January 23, 2016, which may be linked to the formation of the spectrally bright pits nearby. We also observed evidence of deposition in several of these regions by their evolving honeycomb structures, which decreased in visible surface roughness. These changes occurred within Ma'at 3, Serqet, and Seth 1 by January 17, 2016. Similar to observations by Jindal et al. (2022), El-Maarry et al. (2017; 2019) described scarp fronts which previously destroyed Hapi 1's ripple formation had faded by December 2015. Based on this evidence and our own observations of newly deposited material in neighboring regions, we interpreted this fading scarp to indicate local deposition.

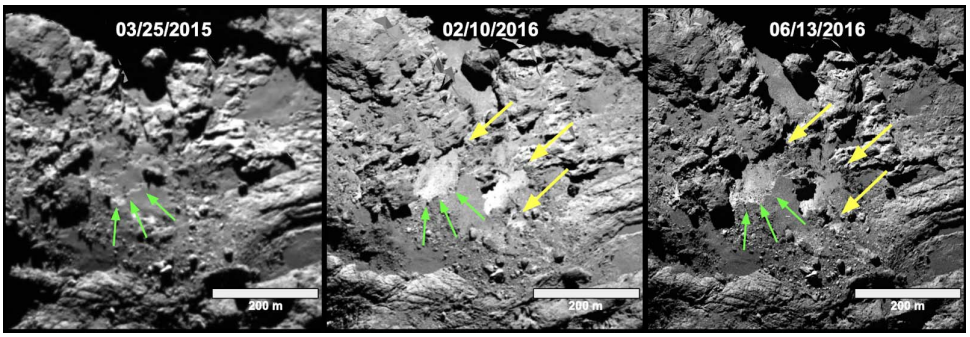

Figure 5. Co-registered images documenting the evolution of bright pits in Khonsu. **Left)** No bright pits were present on March 25, 2015, although some pre-existing structure that created the left pit's boundary can be seen (green arrow). The location of future bright pits is covered under a dust mantle. **Center)** The dust mantle has been eroded to reveal two ~100 meter scale bright pits, and one 10 meter scale bright pit as seen on February 10, 2016 (green arrows indicate the left pit's structural boundary, yellow arrows indicate locations of bright spots). **Right)** The bright pits are still visible on June 13, 2016 (yellow arrows) but they have exhibited an overall reduction in brightness.

3.3.2 Post-Perihelion 2

During Post-Perihelion 2 we observed an increase in erosion in the low latitudes of the northern hemisphere as the subsolar point migrated above the equator. We first detected the new exposure of three locations in Ma'at 3 on the small lobe, which may either be boulders or underlying nucleus. Two of these features had been buried during May, 2015. Almost 2 months after this observation, we identified five more boulder exposures in the southernmost portion of Ma'at 1 on May 9, 2016. On the large lobe, the most significant erosion during this time occurred in Anubis. While we found two boulder migrations and 41 boulder exposures spanning the length of the region on April 10, 2016, uncertainty in their activity date due to resolution limitations indicates activity could have initiated as early as March 2015. It is likely that these boulder exposures were related to the migration of plains in the center of the Anubis region which we observed on September 15, 2015, when the subsolar point would have been passing through the low latitudes of the southern hemisphere. Also on the large lobe, we detected the possible exposure of 7 boulders in Babi 2 on March 13, 2016, although this observation is questionable due to resolution limitations. We also observed the migration of surrounding plains and the exposure of an outcrop of consolidated nucleus in Babi 2 on April 13, 2016, which had been buried by sediment on February 19, 2015. While we only located one boulder migration in Seth 1 on April 28, 2016, we saw less frequent activity in Ash 1. In this region, we detected one boulder exposure, and the formation of 7 quasi-circular pits on April 30, 2016, similar to those that formed within Ma'at 2 during the previous epoch. We identified two more pits forming, although in a different location, within Ash 1 on May 9, 2015. As seen in Ma'at 2, we did not observe these pits growing or migrating after their initial formation, therefore we do not classify them as scarp activity, although they appear to be the result of erosional processing. While we detect no further evidence of sublimation-driven erosion, Deshapriya et al. (2016) documented the formation of a cluster of bright boulders (bright spot 4) on May 7, 2016, which persisted for six weeks after their nominal detection.

As described for several other regions above, we observed that simultaneous deposition and erosion occurred in Anubis during Post-Perihelion 2, with much of the redistributed material possibly sourced from the erosion within Anubis, which was exposed to direct solar insolation at the time. Twelve boulders were buried in Anubis by April 10, 2016, primarily within the same region where migrating plains exposed boulders. On the same date, we detected deposition within the neighboring neck region of Hapi 1 that buried two meter-scale boulders, perhaps suggesting that this infalling sediment may have also come from Anubis. El Maarry et al. (2017; 2019) recorded the fading or partial burial of the a scarp beneath the ripple formation in June, however we detected the fading of this scarp as early as April 10, 2016, coinciding with the deposition which buried the two boulders described above. Finally, El-Maarry et al. (2017; 2019) also recorded decreased surface roughness in honeycombs within Ma'at 3, although we did not identify this activity until June 5, 2016.

3.3.3 Post-Perihelion 3

During Post-Perihelion 3, at distances of >3 AU scarp migration effectively ceased, perhaps due to less energy available to sublimate water ice. In fact, all types of evidence for local erosion and deposition decreased dramatically. An outburst was detected in Imhotep 2 on July 3, 2016 (Vincent et al., 2016; El-Maarry et al., 2019), although this event did not produce visible changes to nearby smooth terrains. While we did detect boulder exposures, migrations, and burials in several regions, these late observations may have been a result of increased resolution

as Rosetta began to orbit closer to 67P's surface. We identified two boulder exposures within a region of migrating plains in Ma'at 2, three boulder exposures and one boulder migration in Ma'at 3, and one sediment slump from smooth materials lying atop a cliff in the northern portion of Ash 3 on June 5, 2016. We observed five boulder exposures within Ash 1 by June 6, 2016, though data coverage and resolution limitations made it difficult to reliably determine when the exposures occurred. We detected 7 boulder exposures in Hapi 1 on June 8, 2016, although similar data limitations suggest that these exposures may have occurred in the previous epoch. Likewise, we located a cluster of 5 boulder exposures in northern Anubis on June 9, 2016 which could have occurred as early as April, 2016. While El-Maarry et al. (2017) showed that the two major pre-existing scarp fronts in Anubis migrated by June, 2016, we show above that these migrations occurred several months earlier, reaching their final positions on November 28, 2015 (Near Perihelion 2). Finally, in Khonsu, the visible brightness waned in the two largest ice-rich pits, although all three pits were still relatively bright compared to neighboring materials on June 13, 2016. This is the last evidence of erosion we detected in 67P's smooth terrains. Deshapriya et al. (2016) indicated that bright spot 2, also located in the Khonsu region, persisted as late as June 24, 2016.

As global erosion decreased, we likewise detected less evidence of ongoing deposition. New smooth deposits buried three boulders within Ma'at 3 by June 5, 2016, and one boulder within Hapi 1 by June 8, 2016. We observed no further evidence of deposition after these dates. As Rosetta began orbiting closer to 67P and eventually crash landed on its surface, images of complete to near complete regions of the comet were no longer available, preventing any further analysis of the comet's meter-to decameter scale surface changes.

4 Discussion

4.1 Key Takeaways

Based on the observations described above, we draw four main conclusions.

1) Sediment is intra- and inter-regionally transported.

While previous models suggest that sediment is first sourced by outgassing in the southern hemisphere (Keller et al., 2015), our observations suggest that significant volumes of sediment are also redistributed intra- and inter-regionally after their initial deposition. As the particles deposited within the smooth terrains are likely rich in water ice (Davidsson et al., 2021), we attribute this localized re-distribution to post-emplacement sublimation of ice retained within the sediment itself.

Evidence of this redistribution began as early as Pre-Perihelion 2, when the scarps migrating through Hapi 2 began to deposit sediment onto the low- and mid-latitudes of the small lobe, primarily in Ma'at 4 and Hatmehit. This process continued into Pre-Perihelion 3, as escalating scarp activity across Hapi 1, 2 and 3 jettisoned even more material, most of which appeared to deposit on top of the small lobe in regions Ma'at 2–4, and to a lesser extent, in Serqet and Maftet (Fig. 6). Later, in Near-Perihelion 1, the energetic scarp-driven activity in the Imhotep 1 basin intra-regionally redistributed grains, burying a boulder, five scarps, and a pit in the process (Jindal et al., 2022). In Near-Perihelion 2, as scarp migrations continued in Imhotep 1, remobilized grains partially or completely buried six scarp fronts in Imhotep 1 and a consolidated cliff in Imhotep 2 (Fig. 7).

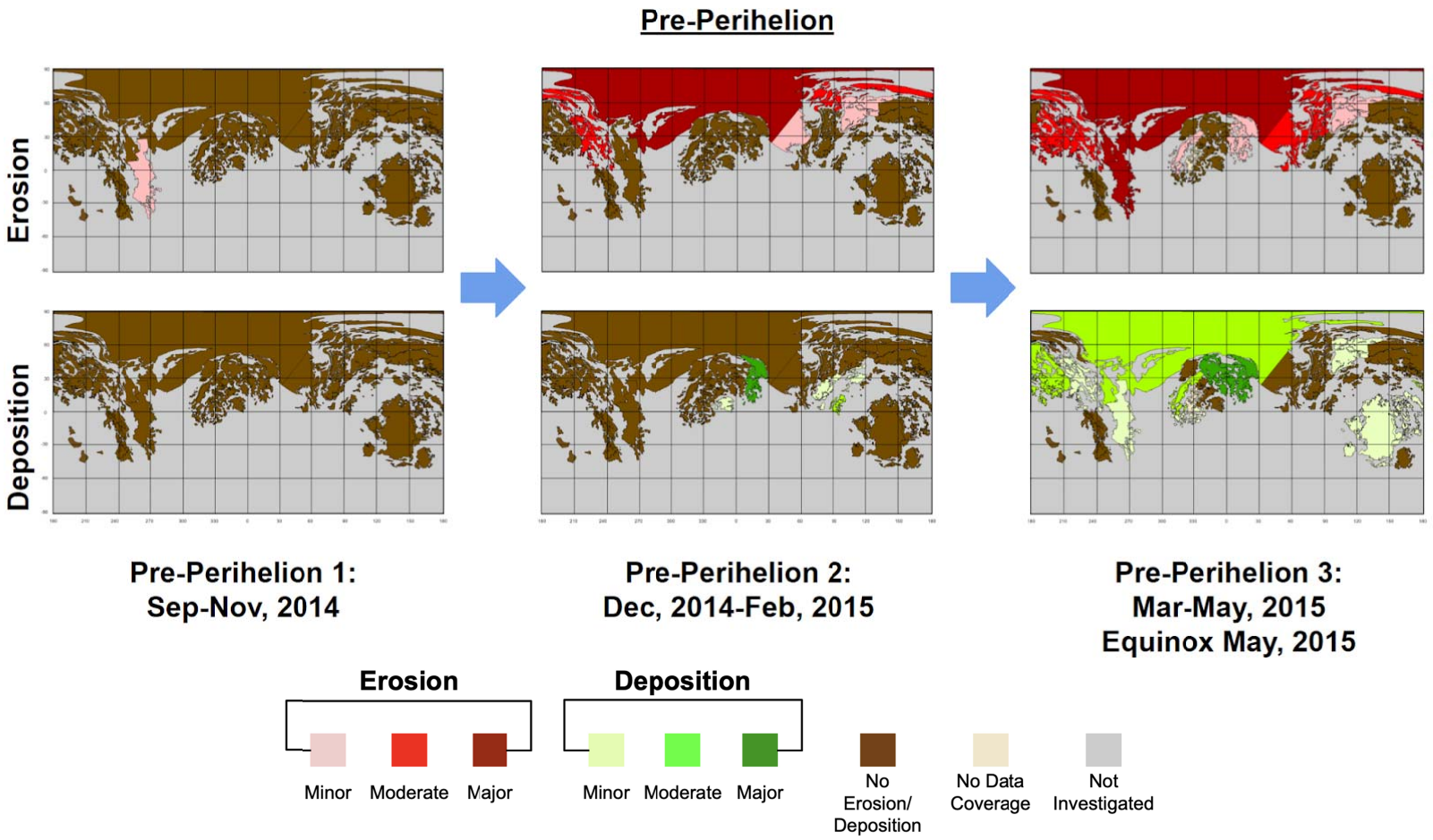

Figure 6. Equirectangular projections of smooth terrain activity in 67P organized to show the progression of erosion (**top**) and deposition (**bottom**) across three pre-perihelion time bins. Each column represents one time bin. Maps on the top/bottom indicate intensity of erosion/deposition. Erosion began in the neck, then also activated in internal regions of the large lobe, followed by lower latitudes on both lobes. Larger scale deposition occurred during Pre-perihelion 3 in many of the same regions experiencing erosion, with additional deposition occurring on top of the small lobe in Ma'at 2–4.

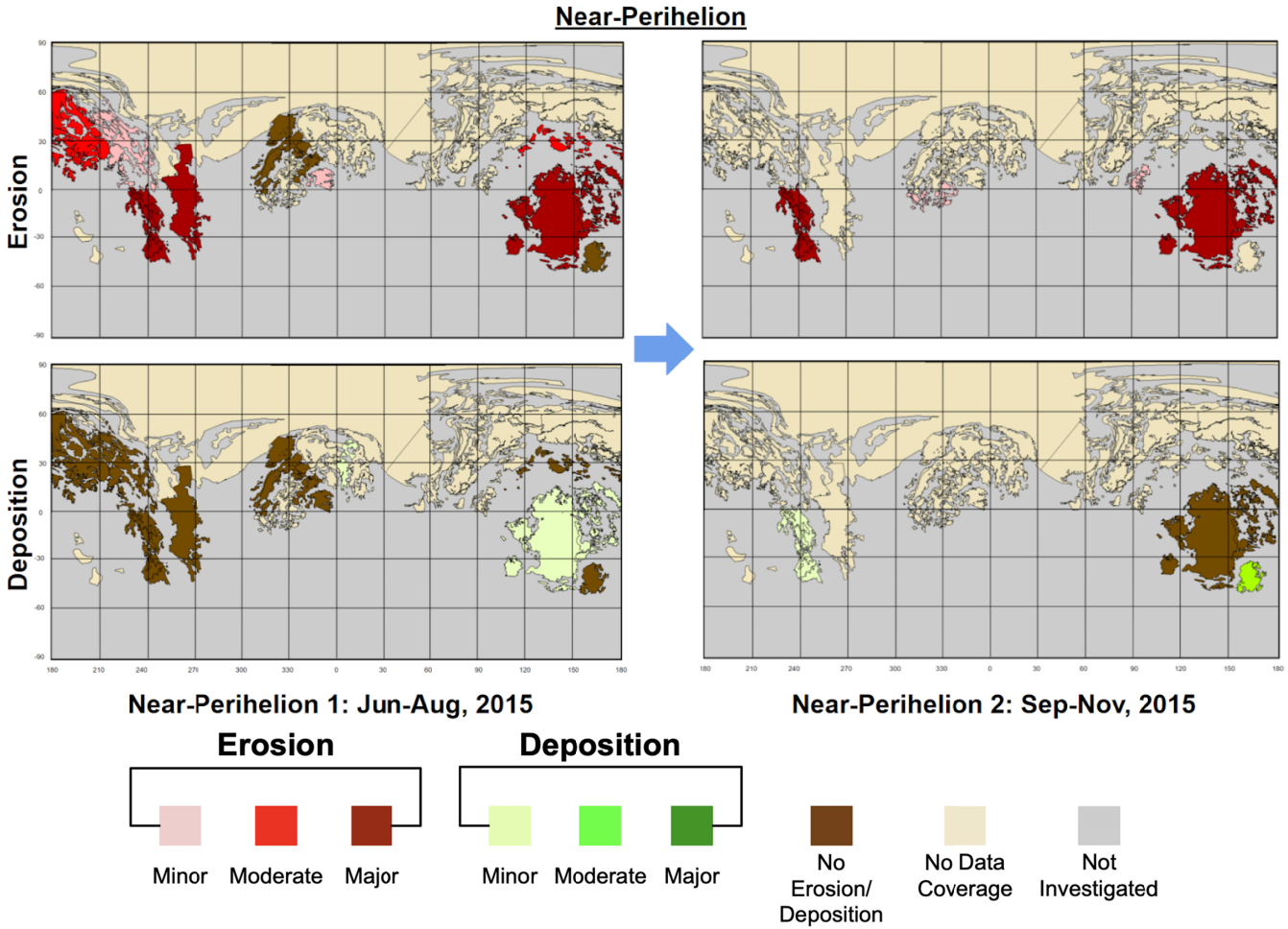

673

674

675 **Figure 7.** Equirectangular projections of smooth terrain activity in 67P organized to show the progression of erosion (**top**) and
676 deposition (**bottom**) across two time bins near 67P's perihelion on August 13, 2015. As a result of decreased image resolution, tan-
677 colored regions were not observable, leaving only the more external regions of the lobe for observation. We observed erosion centered
678 around the mid to low latitudes over these time bins, with some of the eroded material appearing to locally re-distribute. Material from
679 Anubis' scarp migrations appears to fall back into the same region, while sediment lofted from Imhotep 1 appears to deposit both
680 within the same region, and in the nearby alcove of Imhotep 2.

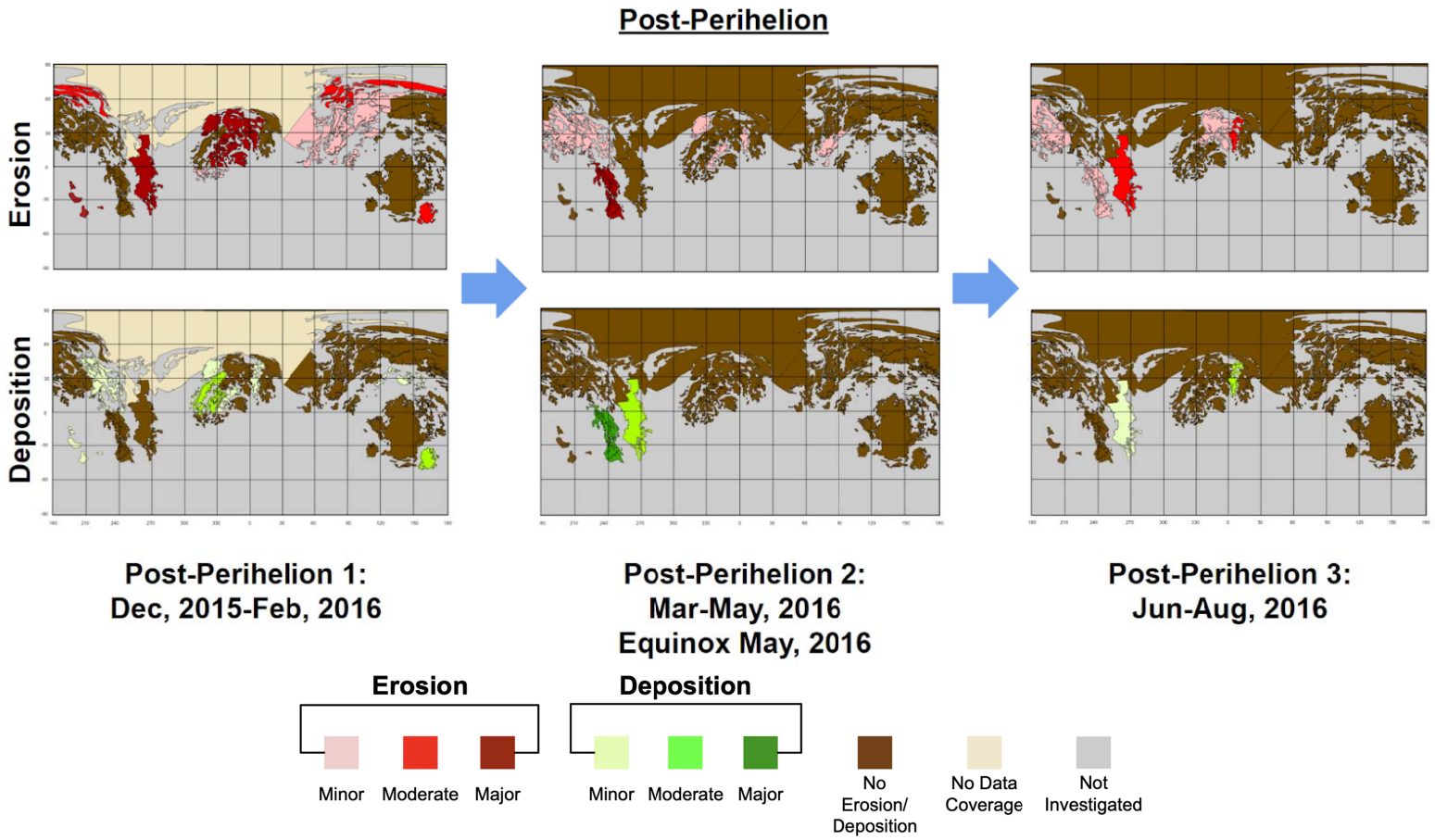

Figure 8. Equirectangular projections of smooth terrain activity in 67P organized to show the progression of erosion (**top**) and deposition (**bottom**) over three time bins occurring after 67P's perihelion passage. As Rosetta returned to lower altitudes, image resolution improved, revealing the majority of the comet surface for observation by March, 2016. Much of the erosion and deposition we observed in the northern hemisphere may have occurred closer to perihelion, as a result of the data limitations shown in Fig. 7. Lower levels of both erosion and deposition continued throughout the remainder of the mission, with spatial trends in the locations of where material was lofted and re-deposited.

Finally, in all Post-Perihelion phases, we observed the redistribution of grains from several sub-regions of Ma'at into Ma'at 3 (Post-Perihelion 1, 2, 3), simultaneous erosion and deposition activity in Khonsu (Post-Perihelion 1) and Anubis (Post-Perihelion 2), and the apparent transport of grains from Anubis to Hapi 1 (Post-Perihelion 2) (Fig. 8).

However, a direct link between the possible sources and sinks of material cannot be definitively established. This is largely the result of the sporadic nature over which Rosetta OSIRIS NAC data were acquired, wherein we lack simultaneous observations of both a source and sink region, or any continuous/quasi-continuous imaging capable of resolving a given sediment transport pathway. Instead, we observe two regions eroding and depositing simultaneously and nearby each other (e.g., Hapi 2 and Ma'at 4 in March–May, 2015), and then infer that sediment is transporting between them. Our observations are therefore consistent, though perhaps not diagnostic, with some amount of intra- and inter-regional sediment redistribution, indicating possible sediment transport pathways by which smooth terrains can rearrange on 67P over time.

2) Erosion and deposition follow the subsolar latitude, and are strongly influenced by local topography.

Observable erosion began in the neck in Hapi 1, spread to the rest of the neck and internal/comet-facing regions, progressed 'southward' onto the tops of the comet's lobes, further south onto the face of either lobe, and finally into the southern hemisphere near perihelion (Fig. 6–9). The southward progression of erosional activity is consistent with the migration of the subsolar latitude as 67P approached perihelion (Keller & Kührt, 2020). Before perihelion, El-Maarry et al. (2019) and Hu et al. (2017) observed honeycomb maturation in the low- and mid-latitudes of Ma'at, Nut and Serqet south of our own observations of erosion. We interpret these honeycomb evolutions to be some of the earliest indicators of local erosion. We also observed evidence of local enhancement due to topographic self-heating in Hapi 2, where the cliffs of Hathor and Seth 2 re-radiated onto the neck, sustaining scarp migration events for over six months. Locations of enhanced activity in the neck and within isolated pits in other regions were modeled by Keller et al. (2015) and are consistent with observed activity in Hapi 2, as well as scarp activity observed in pits from the Ash 1 and Seth 1 regions.

Depositional activity followed a similar, although less direct trend, broadly beginning in regions near the neck and progressing southward, slightly lagging the subsolar latitude. Within any given region, we also observed heterogeneous deposition of new materials, suggesting that sediment transport pathways are often quite short. If we assume the grains initially deposited are water ice-rich (Davidsson et al., 2021), then these local variations could result from two competing effects. First, a given location may have a limited supply of ice-rich sediment, wherein such regions are distant from a given source region or topographic variations block the delivery of new ice-rich particles — quantified via the "deliverability" index of Davidsson et al. (2021). Equally, sediment may either lack the necessary ice needed to re-mobilize sediment due to prolonged exposure during transport/on the surface, or sediment may be relaunched immediately upon deposition — quantified by the "survivability" described in Davidsson et al. (2021).

Topography can therefore both shield a location from receiving new material, but also enhance the local erosion rates of any newly deposited material due to self-heating (Jindal et al., 2022). Given the large topographic variations across the comet, the highly localized nature of erosion and deposition is therefore not surprising. This pattern also suggests a remarkable

terrestrial analog, wherein the topographic evolution of a given portion of 67P's smooth terrains is controlled by the capacity for sediment to be transported, and the supply over which it is delivered. Just as a river adjusts its geometry to varying sediment supplies, so too do 67P's smooth terrains.

3) *Scarp activity is primarily limited to equatorial and internal regions.*

As the primary driver of erosion in the smooth terrains (Birch et al., 2019), scarp activity is influenced both by the subsolar latitude and the presence of surrounding topography. On external portions of the nucleus, topographic relief is lower, and the presence/absence of scarps follows the subsolar latitude (Fig. 10). This trend was most apparent in Imhotep 1 during 67P's perihelion approach, where scarps began migrating in the northern portion of Imhotep 1 in June, 2015. Progressively more southern scarps appeared and began migrating as the comet approached perihelion, consistent with observations by Jindal et al. (2022). By October, 2015, we once again detected scarp migrations in the northern portion of the basin until all migration in Imhotep 1 stopped between November-December, 2015. As a result of this insolation dependence (both direct and re-radiated from surrounding topography), scarp activity was primarily limited to low- to mid-latitudinal regions mostly bordering the equator (Khonsu, Anubis, Hatmehit, Imhotep 1, Ash 4) as 67P approached perihelion.

Meanwhile on internal portions of the comet, the influence of topography becomes especially important. Specifically, any given spot of the surface on internal portions of 67P `sees' significant fractions of the comet above their local horizon (Birch et al., 2019; Jindal et al., 2022). These surfaces then re-radiate onto the smooth terrain regions, providing a secondary heat source that is sufficient to form scarps. This was the case for Hapi 1, Hapi 2, Hapi 3, Seth 1, Seth 2, Babi 1, and Ash 1 (Fig. 10). We also observed examples of re-radiation encouraging scarp formation in the neck and in pits containing smooth terrains in Ash 1 and Seth 1, and Imhotep 1 along several topographic boundaries that acted as discontinuities from which several scarps generated (Fig. S1).

Other smooth terrains on 67P never showed evidence for scarps. In 67P's current orbital configuration, the mid- to high- latitudes (tops of either lobe) were in polar winter as the comet approached perihelion. The subsolar point passed through the lowest latitudes of these regions while the comet was still at distances of >2.5 AU from the Sun, providing much less total solar insolation to the tops of either lobe compared to the other external regions of the comet. Further, these regions lack significant topographic relief and the secondary energy source they provide.

Therefore, as in previous work, we suspect that scarp migration results from the complex interactions between 67P's high relief topography and the local, rapidly changing illumination conditions as 67P approached perihelion. This appears to produce highly localized enhancements in the total amount of energy a given location on the surface receives. Combined with the presence of local re-radiating hot spots like boulders or cliffs within the plains (owing to being more conductive) (Marschall et al., 2017), scarp formation ends up being extremely localized, rather than a simple removal of an upper unconsolidated sedimentary layer (Birch et al., 2019; Jindal et al., 2022). This therefore explains why regions near 67P's north pole, which otherwise receive minimal direct illumination, can still host scarps, while for external regions, only those directly illuminated near perihelion 67P display scarps (Fig. 10).

4) *We observe net zero erosion/deposition on the tops of the lobes, perhaps indicating the presence of terminal sinks for airfalling sediment.*

A final striking pattern we observe is that over 67P's mid-latitudes (30–60° N),which represent the "tops" of each lobe when viewed edge-on, the surface was largely inactive at Rosetta's NAC image resolution (Fig. 11). Although deposition is inherently difficult to discern in the projected images, and the surface could have gained/lost sediment up to ~50 cm depth without our detection (equal to the best resolution Rosetta obtained before/after perihelion), the absence of any activity stands in stark contrast to the rest of the comet. All other regions exhibited at least minor activity and reorganization of the overlying sedimentary cover, while these regions showed almost zero changes of any kind.

The clearest example is Ash 2, where we detected zero deposition or erosion activity of any kind. Also on the large lobe, we observed no activity from 40-60°N in Ash 1, and the mid-latitudinal regions of Babi 1 and Seth 2 (Fig. 11). We likewise identified very limited activity in Ash 3, most of which occurred as slumping of over-steepened mounds of smooth terrains along the margins of overhanging cliffs. While we detected isolated boulder exposures in this region, they were situated on relatively low elevation terraces within the elongated pit of the Aten region. In Ash 3 we likewise identified sediment that coated an outcrop of the underlying nucleus in April, 2015, although the local burial appears to be the result of another gravitational slump of sediment.

We also observe limited surface activity from ~40–50°N latitude on the small lobe (Fig. 11). Similar to Ash 2 and 3, these latitudes of the small lobe experienced polar night for a prolonged period near perihelion. Although boulders and outcrops of consolidated nucleus were exposed in Ma'at 1–4, this erosion all took place below ~40° N, latitudes that never went into polar winter near perihelion. The remaining section of the top of the small lobe appeared unaltered by local erosion, except for one honeycomb evolution in Ma'at 1 that we interpret to be the result of self-heating from a nearby cliff. While we observed changing honeycomb maturity within the rest of Ma'at due to both erosion and deposition, these features were primarily located between 20–40° N latitude (El-Maarry et al., 2019).

The lack of detectable activity in these regions is consistent with previous models. Keller et al., (2015) modeled erosion in these regions and their counterparts on the large lobe and estimated that they should be the least active locations on the comet. Keller et al. (2015) likewise noted that the most active sections of these regions were the sections that slope to the south, consistent with our observations of activity from 20–40° N. Erosion and deposition models from Lai et al. (2016) also suggest that grains from about 0.04–0.08 mm in diameter should have deposited in these regions in January, 2015, but grains from about 0.04–22 mm should have been eroding from the surface in August, 2015. The result of this activity is a net-zero loss of material on the tops of either lobe across all modeled grain sizes (Lai et al., 2016), consistent with our observations.

Despite the limited observed activity and surface changes, these deposits will likely still evolve thermally. Though the upper centimeters of the surface may be exhausted of their ices, material just below the diurnal skin depth could be especially enriched in volatiles if there is even a small degree of net-deposition to buffer and protect these sediments from sublimating their internal ices. Given how stationary grains on these surfaces may be, sintering may also add a small degree of cohesion. Not only would this armor the surface against subsequent erosion and re-mobilization of deposited grains, but it may also set up subsurface stratigraphy.

Specifically, if mixing and granular convection are small, these deposits may have multiple inter-bedded layers that reflect deposition of new material across multiple orbits.
We therefore interpret these regions as terminal sinks for sediment, where the small amounts of airfall grains that meet the surface may not be able to subsequently leave, even near perihelion. Sediment would therefore be transport-limited, and would instead thermally evolve in situ and more slowly than other smooth terrain deposits over many orbits. Such deposits may therefore retain larger ice volumes than other smooth terrain deposits on 67P, making them high value targets for sample return missions. Yet smooth terrains in these regions still bury the underlying topography. The net-zero activity levels then suggest that these near-polar deposits must accumulate extremely slowly, or that these deposits accumulated in a different 'climate' wherein 67P's obliquity was more favorable for a more rapid accumulation. Follow-up sediment transport models should investigate this more rigorously, as well as the potential effects of sintering and the comparative ice depletion of freshly generated vs. redistributed sediments in order to understand when these smooth terrains accumulated their sediment and what that implies for 67P's long-term surface and thermal evolution.

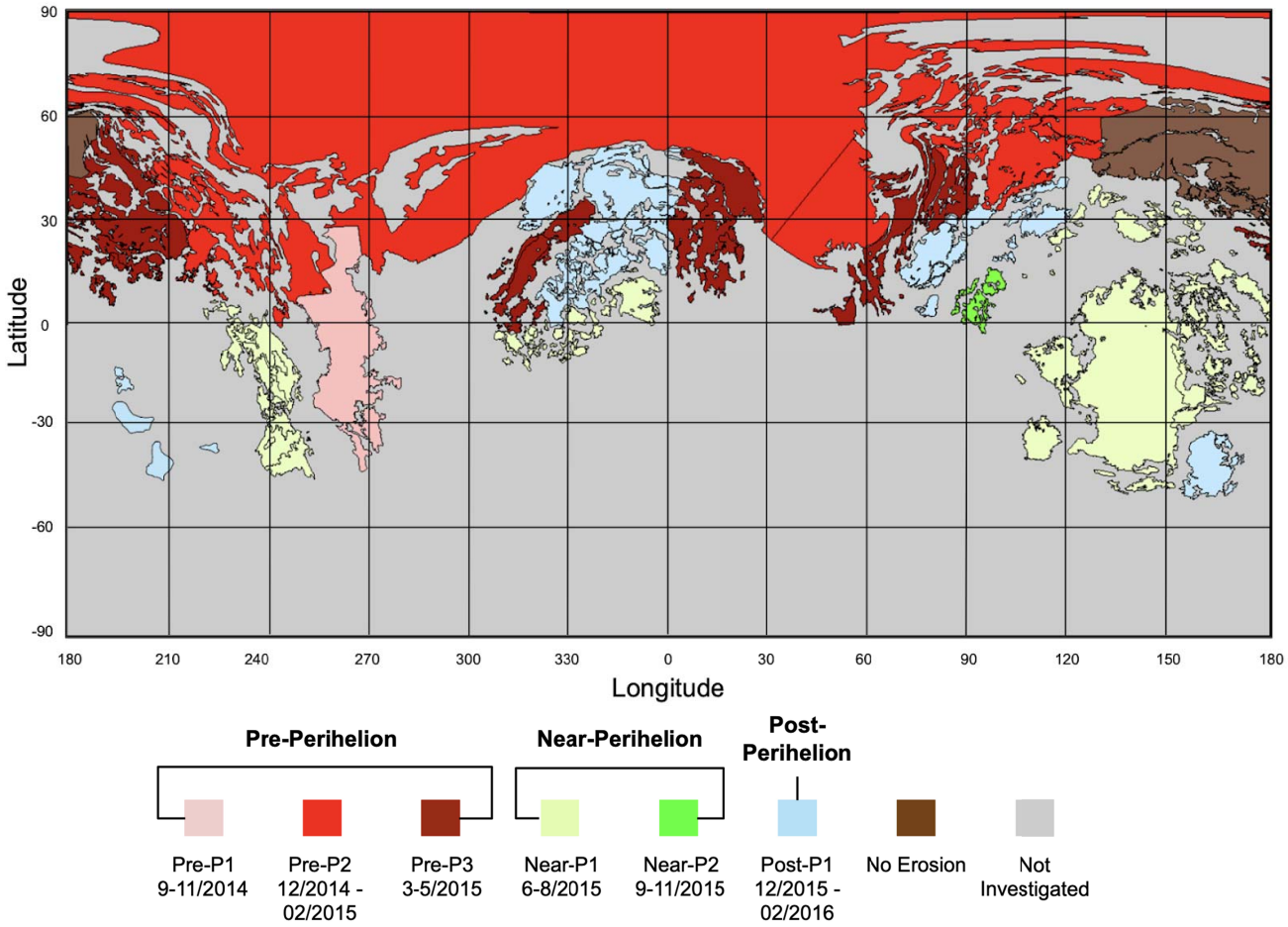

Figure 9. Equatorial projection showing the onset of local erosion by region, color coded to show pre-perihelion (shades of red), near-perihelion (shades of green), and post-perihelion (shades of blue) time bins. Regions in brown show zero evidence of erosion at any point during the period of our observations, while those in gray were not investigated due to a lack of observations or smooth terrains.

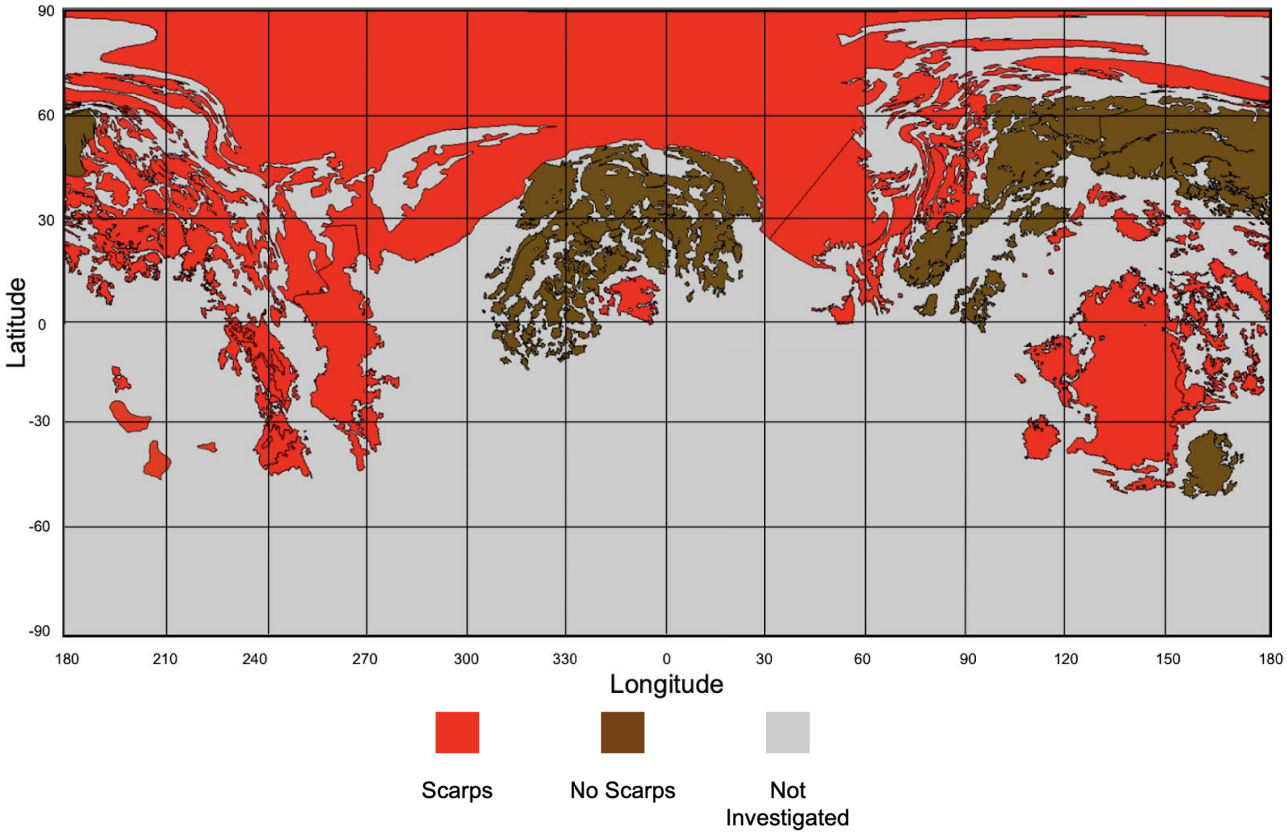

Figure 10. Equatorial projection documenting the distribution of scarp activity across 67P by region. Activity is focused in equatorial regions (~ -30–30° latitude), and internal regions which have increased energy input due to topographic self-heating. Although Ash 1 experienced scarp activity, all active areas of the region occur below 30° latitude.

4.2 Implications for Other Comets

Of the six resolved comets imaged to date, four were viewed with sufficient resolution to analyze the comets' surface morphologies. On all four, we observe smooth terrains over some fraction of their surfaces. While the expression of each of the processes described above may vary, the sublimation-driven evolutionary processes on 67P have both planetary and cometary analogs. Mars's scalloped terrains and swiss cheese terrains (Morgenstern et al., 2007; Lefort, Russell & Thomas 2010), Pluto's pits (Howard et al. 2017), Triton's depressions in its southern hemisphere terrains (Hansen et al. 2021) and even hollows on Mercury (Thomas, Rothery, Conway & Anand, 2014) all exhibit striking similarities to scarp fronts observed on 67P, wherein volatile sublimation liberates refractory grains, driving the back-wasting of scarps. Scarp retreat is also proposed as a mechanism for the growth of Titan's small lake depressions (Hayes et al. 2016), and occurs across Earth where failure at a cliff base, combined with efficient transport of the produced sediment, form a characteristic shape (Howard, 1995). Scalloped features have also been seen on comet 9P/Tempel 1 (Veverka et al., 2013), (Thomas et al., 2013a), providing evidence of previous scarp migrations on other comets. Additionally, comet 9P/Tempel 1's S2 'flow' boundary recession (Thomas et al., 2013a) closely parallels scarp migrations found on 67P, where near surface volatile ices sublimate and cause the recession of a smooth terrain

boundary. While the various expressions of scarp migrations described indicate an influence from various planetary conditions (e.g., gravity, volatile-refractory mixing at the grain scale, presence/absence of an atmosphere, etc.), the underlying physics related to how ice sublimation can initialize the mobilization of grains and result in back-wasting scarp fronts is clearly universal across the solar system.

We also speculate that the honeycomb features may be analogous to sublimation features on Mars such as brain terrain, which form via differential sublimation processes on thermally fractured surfaces (Hu et al., 2017; Mangold et al., 2003). The small scale and variable expression of honeycombs on 67P could be the result of the highly irregular shape of 67P's surface, or due to highly localized subsurface fractures. These may also represent smaller scale textures that exist in larger plains formations, in which case their presence on other comets would depend largely on local topography, and the surface's propensity to fracture. While we have not detected such features on other comet surfaces, such textures may have occurred at scales that were not resolvable. A more detailed study of these features is warranted, as their formation is unique and remains puzzling (Hu et al., 2017).

The process of redistributing smooth terrains via sublimation also likely depends on the physical and compositional parameters of a given comet. Gravity, for example, influences the travel distances of grains. So for comets with equal activity levels, we might expect larger nuclei to have more isolated, thicker deposits of smooth terrains with a larger component of fine grains than smaller comets. Further, larger comets could hold on to more ice-depleted materials since smaller particles rapidly lose their ices (Davidsson et al., 2021). We also expect the obliquity of the comet to influence the distribution of smooth terrains. Objects with a 0° obliquity would likely have smaller smooth terrain deposits centered around one or both of their poles and, excepting regions of gravitational lows, no smooth terrains in the low to mid-latitudes. On the contrary, comets with high obliquity like 67P have larger smooth terrain deposits on the hemisphere that experiences polar winter near perihelion, as re-mobilization at such locations is hampered.

If 67P's obliquity were different in the past, the locations where smooth terrains accumulate/erode may have also been different. These expectations are also consistent with observations of two main regions of smooth deposits observed on comet 9P/Tempel 1, which has gravity ~1.5 times larger than 67P (Richardson, Melosh, Lisse & Carcich, 2007) and an obliquity of 28° (Sekanina, 1981). On comet 9P, we observe one south polar smooth terrain deposit, and two located in gravitational lows (Thomas et al., 2013a). We also observed smooth terrains within the neck of Hartley 2. With ~10 times less gravity than 67P (Thomas et al., 2013b; Sierks et al., 2015; Jia et al., 2017), these potentially larger grains may be more ice-enriched, explaining their observed activity (A'Hearn et al., 2011; Steckloff et al., 2016).

Such questions could be also addressed by future landers, orbiters, and flyby missions on this comet, or many others with varying masses and orbital configurations. Because both gravity, obliquity, and timing of perihelion should strongly affect the location, distribution and composition of smooth terrains, they are vital factors to consider when selecting sample sites for future comet sample return missions.

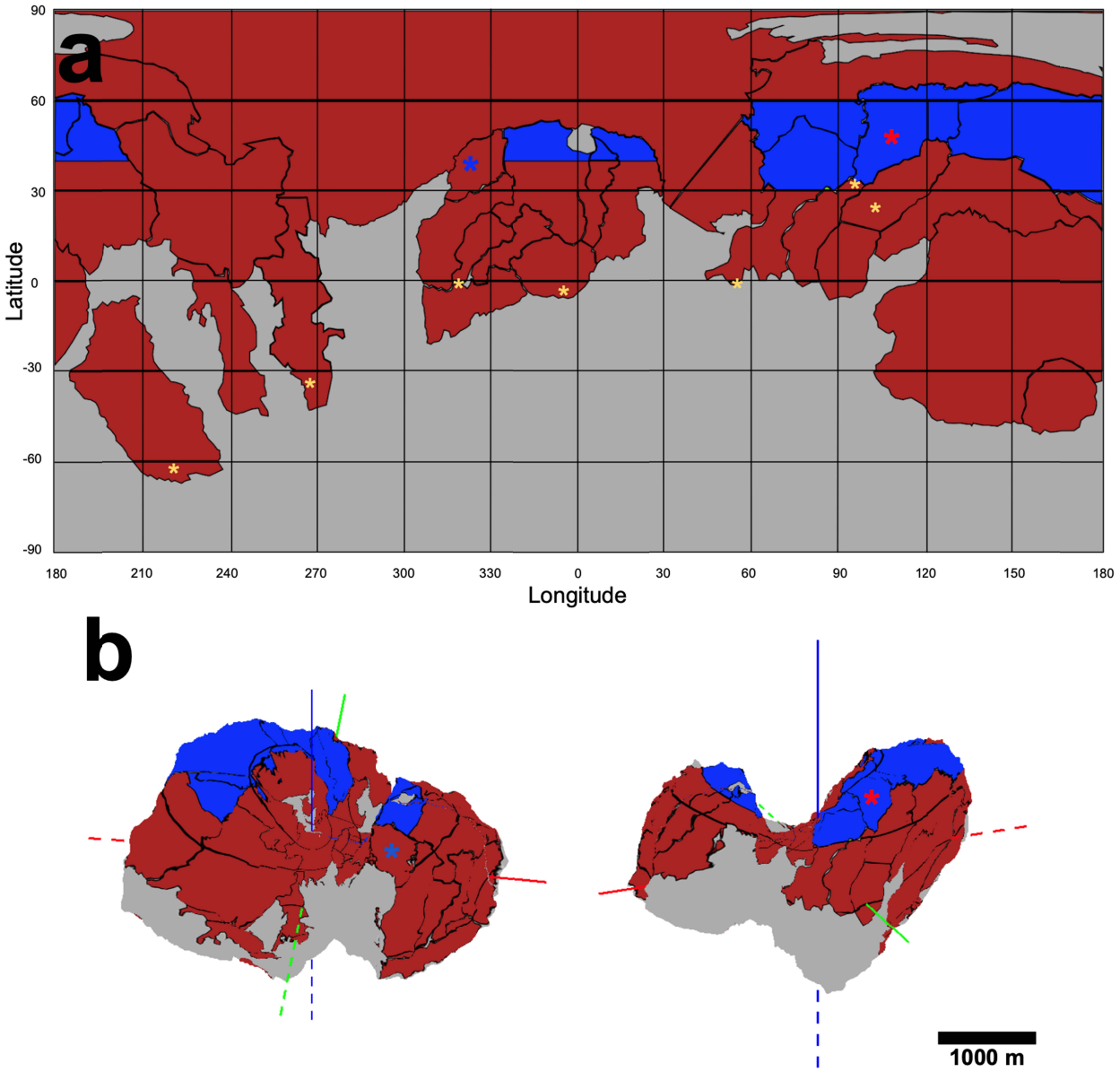

Figure 11. **a**) Equirectangular projection showing latitudes with observed erosional or depositional activity (red), and regions with zero observed activity (blue). Regions are broken into latitude bins of ~30°, except for subregions of Ma'at, which are broken into 10° latitude bins to show inactive areas on the head of the small lobe. Yellow asterisks indicate no activity was observed in the specific latitude bin, but the area is still interpreted as active overall because it resides in a broadly active sub-region. The blue asterisk in Ma'at 1 indicates that we observed very limited and localized erosion which may be connected to topographic influences. We observed no erosion or deposition within the rest of the region, which may therefore largely behave as a part of the small lobe's hypothesized terminal sink. The red asterisk indicates limited activity which appears to be the result of settling of sediment due to gravitational instabilities, rather than the direct result of sublimation activity– we therefore interpret the region to be a part of the large lobe's terminal sink extent. **b**) A 3D projection of the regions interpreted as active (red) or inactive (blue). The Z-axis is shown in blue, the Y-axis in green, and the X-axis in red. Dashed lines indicate the negative axis direction.

5 Conclusions

We draw four primary conclusions based on our observations:

1) Sediment is intra- and inter-regionally transported.

2) Erosion and deposition follow the subsolar latitude, and are strongly influenced by local topography.

3) Scarp activity is primarily limited to equatorial and internal regions.

4) We observe net zero erosion/deposition on the tops of the lobes, perhaps indicating the presence of terminal sinks for airfalling sediment.

The processes acting on 67P's smooth terrains are driven by the sublimation of volatiles from both the consolidated nucleus and the sediment within the comet's smooth terrain deposits. As the comet approached and passed through perihelion, erosional activity followed the subsolar latitude southward. The primary expression of this erosion is scarp migration, which is mainly limited to low-latitude, external regions and regions where topography provides localized heating due to re-radiation (i.e. neck and lobe-facing regions, pits in Ash 1 and Seth 1). The increase in erosion as 67P approached perihelion led to intra- and inter-regional redistribution of sediment within the smooth terrains. This re-distribution confirms that some volatile ices survive the transport process from the consolidated southern hemisphere to the smooth terrain deposits in the north. To sample recently deposited grains sourced directly from the southern hemisphere, collection sites should be selected from more southern smooth terrains where scarp fading and burial can be tracked as indicators of recent deposition (e.g., Imhotep). External regions between ~30–60° N experience polar winter during perihelion. At these northern extents, near-zero net erosion and deposition occurs. In a slightly net-depositional environment, this may create terminal sinks where any deposited sediment is less able to be removed from the surface in 67P's current orbital configuration. Such terminal sinks represent valuable locations that probe the paleoclimate of 67P and may also represent optimal sample collection sites. On other comets, their mass, obliquity, and timing of perihelion will likely affect the formation and location of terminal sinks, and more generally the distribution and composition of smooth terrains.

Acknowledgments

This research was supported by a Rosetta Data Analysis Program grant #80NSSC19K1307 and by the Heising-Simons Foundation (51 Pegasi b Fellowship to S.B.). We would like to acknowledge Björn Davidsson, who provided helpful comments on earlier versions of this manuscript. We would also like to acknowledge the Principal Investigator of the OSIRIS camera on ESA's Rosetta spacecraft, Holger Sierks, and the ESA Planetary Science Archive for the data used in this study. This research has made use of the scientific software ShapeViewer (http://www.comet-toolbox.com/).

Open Research

All raw images are available on ESA's Archive Image Browser (https://imagearchives.esac.esa.int). ShapeViewer 4.0.0 software is publicly available for download at www.comet-toolbox.com. ArcMap software is available at https://www.esri.com/en-us/arcgis/products/arcgis-for-personal-use/buy with registration and fee. All relevant ArcMap projects, shapefiles, layers, and basemaps are available on https://hayesresearchgroup.com/data-products/.

References

A'Hearn, M. F. et al, (2011), EPOXI at Comet Hartley 2, *Science,* 332(6036), 1396-1400. https://doi.org/10.1126/science.1204054

A'Hearn, M. F. et al, (2012), Cometary Volatiles and The Origin of Comets, *The Astrophysical Journal,* 758, 29-36. https://doi.org/10.1088/0004-637X/758/1/29

Belton, M. J. S. et al., (2013), The complex spin state of 103P/Hartley 2: Kinematics and orientation in space. *Icarus*, 222(2), 595-609. https://doi.org/10.1016/j.icarus.2012.06.037

Birch, S. P. D. et al., (2017), Geomorphology of comet 67P/Churyumov-Gerasimenko, *Monthly Notices of the Royal Astronomical Society*, 469(Suppl_2), S50-S67. https://doi.org/10.1093/mnras/stx1096

Birch, S. P. D. et al., (2019), Migrating Scarps as a Significant Driver for Cometary Surface Evolution, *Geophysical Research Letters,* 46(22), 12794-12804. https://doi.org/10.1029/2019GL083982

Brownlee, D. E. et al., (2004), Surface of young Jupiter family comet 81P/Wild 2: View from the Stardust spacecraft, *Science*, 304(5678), 1764-1769. https://doi.org/10.1126/science.1097899

Davidsson, B. J. R. et al., (2021), Airfall on Comet 67P/Churyumov-Gerasimenko, *Icarus,* 354, 114004. https://doi.org/10.1016/j.icarus.2020.114004

Deshapriya, J. D. P. et al., (2016), Spectrophotometry of the Khonsu region on the comet 67P/Churyumov–Gerasimenko using OSIRIS instrument images, *Monthly Notices of the Royal Astronomical Society*, 462(Suppl_1), S274–S286. https://doi.org/10.1093/mnras/stw2530

El-Maarry, M. R. et al., (2015), Regional surface morphology of comet 67P/Churyumov-Gerasimenko from Rosetta/OSIRIS images, *Astronomy & Astrophysics*, 583, A26. https://doi.org/10.1051/0004-6361/20152573

El-Maarry, M. R. et al., (2017), Surface Changes on Comet 67P/Churyumov-Gerasimenko Suggest a More Active Past, *Science*, 355(6332), 1392-1395. https://doi.org/10.1126/science.aak9384

El-Maarry, M. R. et al., (2019) Surface Morphology of Comets and Associated Evolutionary Processes: A Review of Rosetta's Observations of 67P/Churyumov–Gerasimenko, *Space Science Review,* 215, 36. https://doi.org/10.1007/s11214-019-0602-1

1004 Fornasier, S. et al., (2015), Spectrophotometric properties of the nucleus of comet
1005 67P/Churyumov-Gerasimenko from the OSIRIS instrument onboard the ROSETTA spacecraft,
1006 *Astronomy & Astrophysics*, 583, A30. https://doi.org/10.1051/0004-6361/201525901
1007 Hansen, C. J. et al., (2021), Triton: Fascinating Moon, Likely Ocean World, Compelling
1008 Destination!, *Planetary Science Journal*, 2(4), 137-148. https://doi.org/10.3847/PSJ/abffd2
1009 Hortsman, K. C., Melosh, H. J., (1989) Drainage pits in cohesionless materials: implications for
1010 surface of Phobos. *Journal of Geophysical Research*, 94 (B9), 12433-12441.
1011 https://doi.org/10.1029/jb094ib09p12433
1012 Howard, A. D. (1995). Simulation modeling and statistical classification of escarpment
1013 planforms. *Geomorphology,* 12(3), 187–214. https://doi.org/10.1016/0169-555X(95)00004-O
1014 Howard, A. D. et al., (2017). Pluto: Pits and mantles on uplands north and east of Sputnik
1015 Planitia, *Icarus*, 293, 218-230. https://doi.org/10.1016/j.icarus.2017.02.027
1016 Hu, X. et al., (2017), Seasonal erosion and restoration of the dust cover on comet
1017 67P/Churyumov-Gerasimenko as observed by OSIRIS onboard Rosetta, *Astronomy &*
1018 *Astrophysics*, 604, A114. https://doi.org/10.1051/0004-6361/20162990
1019 Jia, P., Andreotti, B., and Claudin, P. (2017), Giant ripples on comet 67P/Churyumov-
1020 Gerasimenko sculpted by sunset thermal wind, *PNAS,* 114(10), 2509-2514.
1021 https://doi.org/10.1073/pnas.1612176114
1022 Jindal, A. S. et al., (2022), Topographically Influenced Evolution of Large-scale Changes in
1023 Comet 67P/Churyumov–Gerasimenko's Imhotep Region, *Planetary Science Journal*, 3,
1024 193. https://doi.org/10.3847/PSJ/ac7e48
1025 Keller, H. U. et al., (1986) First Halley Multicolour Camera imaging results from Giotto,
1026 *Nature,* 321, 320-326. https://doi.org/10.1038/321320a0
1027 Keller, H. U. et al., (2007), OSIRIS--The Scientific Camera System Onboard Rosetta, *Space*
1028 *Science Reviews*, 128, 433-506. https://doi.org/10.1007/s11214-006-9128-4
1029 Keller, H. U. et al., (2015) Insolation, erosion, and morphology of comet 67P/Churyumov-
1030 Gerasimenko, *Astronomy & Astrophysics*, 583, A34.
https://doi.org/10.1051/0004-6361/201525964
1031 Keller, H. U. et al., (2017), Seasonal mass transfer on the nucleus of comet 67P/Churyumov–
1032 Gerasimenko, *Monthly Notices of the Royal Astronomical Society*, 469(Supple_2), S357–
1033 S371. https://doi.org/10.1093/mnras/stx1726
1034 Keller, H. U. & Kührt, E. (2020), Cometary Nuclei—From Giotto to Rosetta, *Space Science*
1035 *Reviews,* 216, 14. https://doi.org/10.1007/s11214-020-0634-6
1036 Lauretta, D. S., et al., (2018), The CAESAR New Frontiers Mission: 2. Sample Science. In *49th*
1037 *Lunar and Planetary Science Conference*, The Woodlands, TX, Contribution Number 2083.
1038 Lefort, A., Russell, P. S., & Thomas, N., (2010), Scalloped terrains in the Peneus and
1039 Amphitrites Paterae region of Mars as observed by HiRISE, *Icarus*, 205(1), 259-
1040 268. https://doi.org/10.1016/j.icarus.2009.06.005
1041 Lisse C. M. et al., (2009), Spitzer Space Telescope Observations of the Nucleus of Comet
1042 103P/Hartley 2, *Publications of the Astronomical Society of the Pacific,* 121(883), 968-
1043 975. https://doi.org/10.1086/605546
1044 Marschall, R. et al., (2017), Cliffs versus plains: Can ROSINA/COPS and OSIRIS data of comet
1045 67P/Churyumov-Gerasimenko in autumn 2014 constrain inhomogeneous outgassing?,
1046 *Astronomy & Astrophysics*, 605, A112. https://doi.org/10.1051/0004-6361/201730849
1047 Maquet, L. (2015), The recent dynamical history of comet 67P/Churyumov-Gerasimenko,
1048 *Astronomy & Astrophysics,* 579, A78. https://doi.org/10.1051/0004-6361/20142541

1049 Mousis, O. et al., (2015), Pits Formation from Volatile Outgassing on 67P/Churyumov-
1050 Gerasimenko, *The Astrophysical Journal Letters,* 814(1), L5. https://doi.org/10.1088/2041-
1051 8205/814/1/L5
1052 Oklay, N. et al., (2016), Variegation of comet 67P/Churyumov-Gerasimenko in regions showing
1053 activity, Astronomy & Astrophysics, 586, A80. https://doi.org/10.1051/0004-6361/20152739
1054 Pajola, M. et al., (2016), Aswan site on comet 67P/Churyumov–Gerasimenko: morphology,
1055 boulder evolution, and spectrophotometry. *Astronomy & Astrophysics*. 592, A69.
https://doi.org/10.1051/0004-6361/20152785
1056 Pajola, M. et al., (2017), The pebbles/boulders size distributions on Sais: *Rosetta*'s final landing
1057 site on comet 67P/Churyumov–Gerasimenko, *Monthly Notices of the Royal Astronomical*
1058 *Society,* 469(Suppl_2), S636-S645. https://doi.org/10.1093/mnras/stx1620
1059 Reinhard, R., (1986), The Giotto Encounter with Comet Halley, *Nature,* 321, 313-318.
1060 https://doi.org/10.1038/321313a0
1061 Richardson, J. E., Melosh, H. J., Lisse, C.M., & Carcich, B., (2007), A ballistics analysis of the
1062 Deep Impact ejecta plume: Determining Comet Tempel 1's gravity, mass, and density, *Icarus,*
1063 191(2), Supplement, 176-209. https://doi.org/10.1016/j.icarus.2007.08.033
1064 Sekanina, Z., (1981), Rotation and Precession of Cometary Nuclei, *Annual Review of Earth and*
1065 *Planetary Sciences,* 9, 113-145. https://doi.org/10.1146/annurev.ea.09.050181.000553
1066 Shi, X., et al., (2016), Sunset jets observed on comet 67P/Churyumov-Gerasimenko sustained by
1067 subsurface thermal lag, *Astronomy & Astrophysics*, 586, A7. https://doi.org/10.1051/0004-
1068 6361/201527123
1069 Sierks, H. et al., (2015), On the nucleus structure and activity of comet 67P/Churyumov-
1070 Gerasimenko, Science, 347(6220), 1044. https://doi.org/10.1126/science.aaa1044
1071 Sodorblom, L. A. et al., (2002), Observations of comet 19/Borrelly by the miniature integrated
1072 camera and spectrometer aboard Deep Space 1, *Science*, 296(5570), 1087-1091.
1073 https://doi.org/10.1126/science.1069527
1074 Squyres, S. W. et al., (2018) The CAESAR New Frontiers Mission: 1. Overview, In *49th Lunar*
1075 *and Planetary Science Conference*, The Woodlands, TX, Contribution Number 2083.
1076 Steckloff, J. K. et al., (2016), Rotationally induced surface slope-instabilities and the activation
1077 of CO2 activity on comet 103P/Hartley 2, *Icarus,* 272, 60-69.
1078 https://doi.org/10.1016/j.icarus.2016.02.026
1079 Sunshine, J. M., Thomas, N., El-Maarry, M. R., and Farnham, T. L., (2016), Evidence for
1080 Geologic Processes on Comets, *J. Geophys. Res. Planets*, 121(11), 2194-
1081 2210. https://doi.org/10.1002/2016JE005119
1082 Thomas, N. et al., (2015), The morphological diversity of comet 67P/Churyumov-Gerasimenko,
1083 *Science*, 347(6220), aaa0440. https://doi.org/10.1126/science.aaa0440
1084 Thomas, N et al., (2015b), Redistribution of particles across the nucleus of comet
1085 67P/Churyumov-Gerasimenko, *Astronomy & Astrophysics*, 583, A17.
1086 https://doi.org/10.1051/0004-6361/20152609
1087 Thomas, P. C. et al., (2013a), The nucleus of comet 9P/Tempel 1: Shape and geology from two
1088 flybys, *Icarus*, 222(2), 453-466. https://doi.org/10.1016/j.icarus.2012.02.037
1089 Thomas, P. C. et al., (2013b), Shape, density, and geology of the nucleus of comet 103P/Hartley
1090 2, *Icarus*, 222(2), 550-558. https://doi.org/10.1016/j.icarus.2012.05.034
1091 Thomas, R. J., Rothery, D. A., Conway, S. J., & Anand, M. (2014), Hollows on Mercury:
1092 Materials and mechanisms involved in their formation, *Icarus,* 229, 221-235.
1093 https://doi.org/10.1016/j.icarus.2013.11.018

1094 Tsou, P. et al., (2004), Stardust encounters comet 81P//Wild 2, *Journal of Geophysical Research*,
1095 109(E12), S01. https://doi.org/10.1029/2004JE002317
1096 Veverka, J. et al., (2013), Return to comet Tempel 1: Overview of Stardust NExT results, *Icarus*,
1097 222 (2), 424-435. https://doi.org/10.1016/j.icarus.2012.03.034
1098 Vincent, J.-B. et al., (2015), Large heterogeneities in comet 67P as revealed by active pits from
1099 sinkhole collapse, *Nature,* 523, 63-66. https://doi.org/10.1038/nature14564
1100 Vincent, J.-B. et al., (2016), Summer fireworks on comet 67P, *Monthly Notices of the Royal*
1101 *Astronomical Society*, 462(Suppl_1), S184-S194. https://doi.org/10.1093/mnras/stw2409
1102 Vincent, J.-B. et al. (2018), ShapeViewer, a software for the scientific mapping and
1103 morphological analysis of small bodies,*49th Lunar and Planetary Science Conference*, Abstract
1104 #1281.